

# Studies of noctilucent clouds from the stratosphere during the 2024 TRANSAT balloon flight

Peter Dalin<sup>1</sup>, Hidehiko Suzuki<sup>2</sup>, Nikolay Pertsev<sup>3</sup>, Vladimir Perminov<sup>3</sup>, Linda Megner<sup>4</sup>, Johan Kero<sup>1</sup>, Peter Voelger<sup>1</sup>, Jonas Hedin<sup>4</sup>, Gerd Baumgarten<sup>5</sup>, Anne Réchou<sup>6</sup>, Denis Efremov<sup>7</sup>

<sup>1</sup> Swedish Institute of Space Physics, Kiruna, Sweden

<sup>2</sup> School of Science and Technology, Meiji University, Kawasaki, Japan

<sup>3</sup> A.M. Obukhov Institute of Atmospheric Physics RAS, Moscow Russia

<sup>4</sup> Department of Meteorology (MISU), Stockholm University, Stockholm, Sweden

<sup>5</sup> Leibniz Institute of Atmospheric Physics, Rostock University, Kühlungsborn, Germany

<sup>6</sup> Lacy Laboratory of Atmosphere and Cyclones, Université de La Réunion, Réunion, France

<sup>7</sup> Aerospace Laboratory “Stratonautica”, Moscow, Russia

*Correspondence to:* Peter Dalin (pdalin@irf.se)

**Abstract.** A transatlantic scientific balloon flight (TRANSAT) was conducted between 22 and 26 June 2024. The TRANSAT balloon, operated by the French Space Agency (CNES), floated in the stratosphere at approximately 40 km altitude between Esrangle (Sweden) and Baffin Island (Canada) for about 3.8 days. The scientific payload comprised nine instruments, including two from the Swedish Institute of Space Physics: an optical imager for noctilucent cloud (NLC) studies and an infrasound instrument for atmospheric infrasound wave investigations. The NLC imager consisted of three identical visible-range optical cameras, one of which operated successfully throughout the entire flight, capturing thousands of NLC images. The TRANSAT balloon campaign was supported by ground-based lidar measurements and spaceborne observations from the Swedish MATS satellite. Here, we describe the technical characteristics of the balloon experiment and present early results. Nearly continuous observations of NLC were obtained during the entire flight. A localized warm region in the mesopause was identified as the cause of temporary NLC disappearance, while complex NLC structures exhibiting different motions were found to probably result from horizontal wind rotation with altitude within the mesopause region.

## 1 Introduction

Noctilucent clouds (NLC) are the highest clouds in the Earth’s atmosphere, forming in the summer mesopause region between 80 and 90 km altitude at middle and polar latitudes in both hemispheres. They consist of water-ice particles with radii of 30–100 nm that scatter sunlight, making the clouds visible against the twilight sky. NLCs are typically observed from May to September in the Northern Hemisphere and from November to February in the Southern Hemisphere (Gadsden and Schröder, 1989; Liu et al., 2016). When observed from space, these clouds are traditionally called Polar Mesospheric Clouds (PMC) (Thomas, 1984).

38 NLC and PMC are systematically studied using ground-based optical cameras, spectrographs, lidars as well  
39 as dedicated spaceborne instruments (e.g., Karlsson and Gumbel, 2005; Dalin et al., 2008; Bailey et al., 2009;  
40 Fiedler et al., 2011; DeLand and Thomas, 2015; Tsuda et al., 2022; Wallis et al., 2025). In addition, irregular  
41 campaign-based NLC observations are carried out using sounding rockets and aircraft (Zadorozhny et al., 1993;  
42 Gumbel and Witt, 2001; Reimuller et al., 2011; Suzuki et al., 2022; Pertsev et al., 2024). Each observational  
43 technique has specific advantages and limitations. In particular, ground-based imagers offer high horizontal (~20  
44 m) and temporal (~1 s) resolution (Dalin et al., 2010; Baumgarten and Fritts, 2014), and lidars provide high  
45 vertical resolution (50–150 m; Baumgarten et al., 2009), but both are restricted by tropospheric weather and  
46 limited geographic coverage. Conversely, satellite observations deliver global PMC coverage but suffer from  
47 low spatial (~1 km) and temporal (minutes to hours) resolution. Moreover, sun-synchronous satellites introduce  
48 large spatial gaps (hundreds of km) between adjacent orbits at mid- and subpolar latitudes (45–60°N) due to a  
49 spacecraft orbiting the Earth. Consequently, no single existing technique can fully resolve the microphysical and  
50 dynamical processes governing NLC/PMC.

51 Balloon-borne observations from stratospheric altitudes (25–40 km) have a potential for comprehensive  
52 studies of NLC on a regular basis. Such observations provide several advantages: independence from  
53 tropospheric weather, uninterrupted 24 h coverage, and proximity to the NLC layer (80–85 km), yielding the  
54 highest achievable spatial resolution. From this vantage point, both large-scale (up to 2500 km, limited by  
55 Earth's curvature) and small-scale (down to meters) NLC features can be observed. Furthermore, balloon-borne  
56 observations at 30–40 km altitude occur above the ozone-rich layer (20–25 km), thereby avoiding light  
57 absorption in the Chappuis band (400–650 nm).

58 To date, four balloon-borne experiments have been dedicated to NLC observations from the stratosphere  
59 (Miller et al., 2015; Dalin et al., 2019, 2020, 2022; Fritts et al., 2019). These missions have provided unique  
60 datasets for studying both large- and small-scale wave dynamics and turbulence within NLC layers. In this study,  
61 we present results from a new long-duration balloon experiment aimed at investigating NLC in the polar  
62 mesopause. **The motivation for the NLC experiment on board the 2024 TRANSAT flight are as follows:**

63 **1. Investigation of temporal-spatial variability of NLC at large- and small-scales in the subpolar and**  
64 **polar mesopause for several days.**

65 **2. Quantification of atmospheric gravity waves at large- and small-scales and turbulent processes,**  
66 **with modeling of propagation pathways and search for wave sources in the underlying atmosphere.**

67 **3. Gaining experience in conducting experiments in the stratosphere for several days.**

68 We describe the observation technique and instrumentation as well as early scientific findings. The  
69 stratospheric NLC observations were complemented by ground-based lidars and, for the first time, by  
70 spaceborne measurements from the Swedish MATS satellite. Additionally, temperature and water vapor data  
71 from the Aura/MLS satellite were used to characterize the mesopause environment during the TRANSAT flight,  
72 and JAWARA model data were employed to simulate the thermodynamic and wind conditions in support of the  
73 NLC observations.

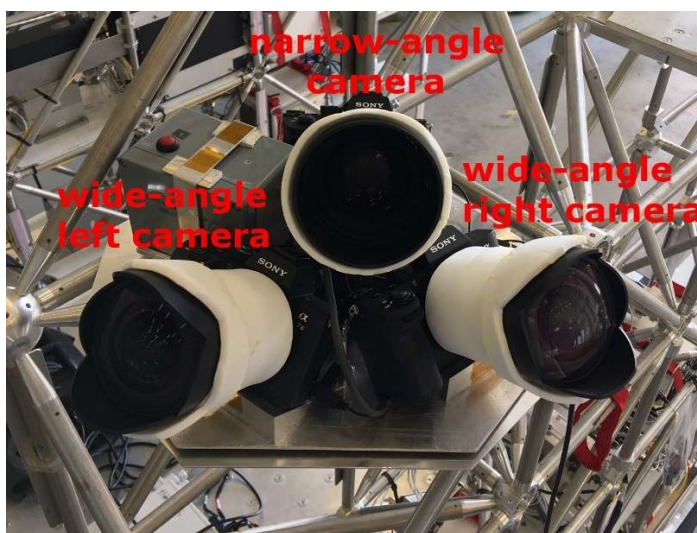
## 74 **2 Technique and method**

### 75 **2.1 Technical characteristics of the imager**

76 The Stratospheric Observations of Noctilucent Clouds (SONC) experiment is a balloon-borne scientific  
77 mission designed to investigate NLC dynamics across a broad range of spatial scales—from large-scale

78 structures (30–2500 km) to fine-scale features (5 m–30 km)—as well as the microphysical properties of NLC ice  
 79 particles.

80 To achieve these objectives, three high-resolution, high-sensitivity Sony  $\alpha 7$  Mark III cameras were used.  
 81 Each camera has a full-frame 35 mm, 24-megapixel sensor ( $6000 \times 4000$  pixels). Two cameras were equipped  
 82 with wide-angle lenses (field of view, FoV,  $=105.4^\circ \times 81.8^\circ$ ), while the third carried a narrow-angle lens  
 83 (FoV= $15.0^\circ \times 10.1^\circ$ ). This configuration, two wide-angle and one narrow-angle camera, provides a horizontal  
 84 coverage of about  $180^\circ$  for studying mesospheric NLC structures up to 2500 km across, while simultaneously  
 85 enabling spatial resolution as fine as about 5 m when viewing the NLC layer at 83 km from a 40 km altitude and  
 86  $35^\circ$  elevation angle. Note that such simultaneous access to both large and small scales is currently unattainable  
 87 from either ground-based or satellite platforms. The three cameras formed the SONC imager, illustrated in Fig.  
 88 1. Each camera stored data on two 1 TB SD cards. Given the expected 4–5 day duration of the transatlantic flight  
 89 and the storage limits, an image acquisition cadence of 50 s was chosen. This temporal resolution enables  
 90 tracking the evolution of small-scale wave activity within the NLC layer as well as monitoring large-scale cloud  
 91 dynamics. The optical axes of the two wide-angle cameras were inclined at  $36^\circ$  to the horizontal plane in order to  
 92 minimize light contamination from bright tropospheric scattering and from above coming from a big white  
 93 balloon envelope ( $\sim 70$  m in diameter). The narrow-angle camera was tilted at  $35^\circ$  to the horizontal plane to  
 94 resolve fine-scale structures of NLC.



95  
 96 **Figure 1: The SONC imager consists of three Sony  $\alpha 7$  Mark III cameras and the electronic control unit**  
 97 **(gray box with red button). Two cameras are equipped with wide-angle lenses, and one with a narrow-**  
 98 **angle lens positioned between them. The instrument was used to observe noctilucent clouds during the**  
 99 **TRANSAT transatlantic balloon flight (22–26 June 2024).**

100  
 101 **Sony  $\alpha 7$  Mark III camera has a standard Micro USB terminal for power supplying, battery charging**  
 102 **and USB communications, into which an external trigger can be connected to activate the shutter button.**  
 103 **For this purpose, we have developed an external trigger (gray box shown in Fig. 1) that simultaneously**  
 104 **transmits the trigger signal to all three NLC cameras at a certain cadence time (50 s in this experiment).**  
 105 **Thus, automatic shooting is carried out by the three cameras throughout the balloon flight. In addition,**  
 106 **this external device distributes power to all three cameras from an external power supply (a chemical**  
 107 **battery on the gondola).**

Automatic exposure bracketing was applied, capturing 5 images sequentially with exposure times varying between 1/1600 s and 1.6 s. This approach accommodated a wide dynamic range of NLC brightness under variable atmospheric background illumination conditions. One wide-angle camera (left in Fig. 1) operated flawlessly throughout the 3.8-day flight, producing a total of about 40,000 images. The other wide-angle and the narrow-angle cameras functioned for the first 13 h and 12 h, respectively, before ceasing operation for unknown reasons. The imager survived the gondola landing on the ice of Baffin Island without damage. Post-flight tests of all the cameras and electronics confirmed full functionality of the SONC imager and no performance degradation. **It should be noted that all three cameras had already been in the stratosphere for about 13 hours at low temperatures of -30°C and were functioning normally (Dalin et al., 2022). Taking into account the previous positive balloon-borne experiment, it was decided to use all three cameras for the long-duration TRANSAT flight in the stratosphere. Also note that SONY  $\alpha$ 7 Mark III cameras are commercial cameras that are not designed for a flight in the stratosphere in 24/7 sunlight, at low temperatures and low thermal conductivity due to rarefied air. The electronics inside the two cameras could freeze or overheat. This is the most likely reason for the failure of these two cameras after 12 h of the flight.**

123

## 124 2.2 Technical characteristics of the TRANSAT balloon flight

125 The TRANSAT mission is a long-duration stratospheric balloon flight organized and operated by the French  
126 Space Agency (CNES) (<https://cnes.fr/en/news/balloons-crossing-atlantic-wind> [https://stratocat.com.ar/fichas-](https://stratocat.com.ar/fichas-e/2024/KRN-20240622.htm)  
127 [e/2024/KRN-20240622.htm](https://stratocat.com.ar/fichas-e/2024/KRN-20240622.htm)) for multidisciplinary atmospheric and cosmic research. The gondola, named  
128 Carmen, had a total mass of about 900 kg and carried nine scientific instruments. Two of these were from  
129 Sweden: the SONC imager and an infrasound instrument dedicated to studies of infrasound atmospheric waves  
130 and their sources. The infrasound experiment and its scientific results will be described in a separate paper.

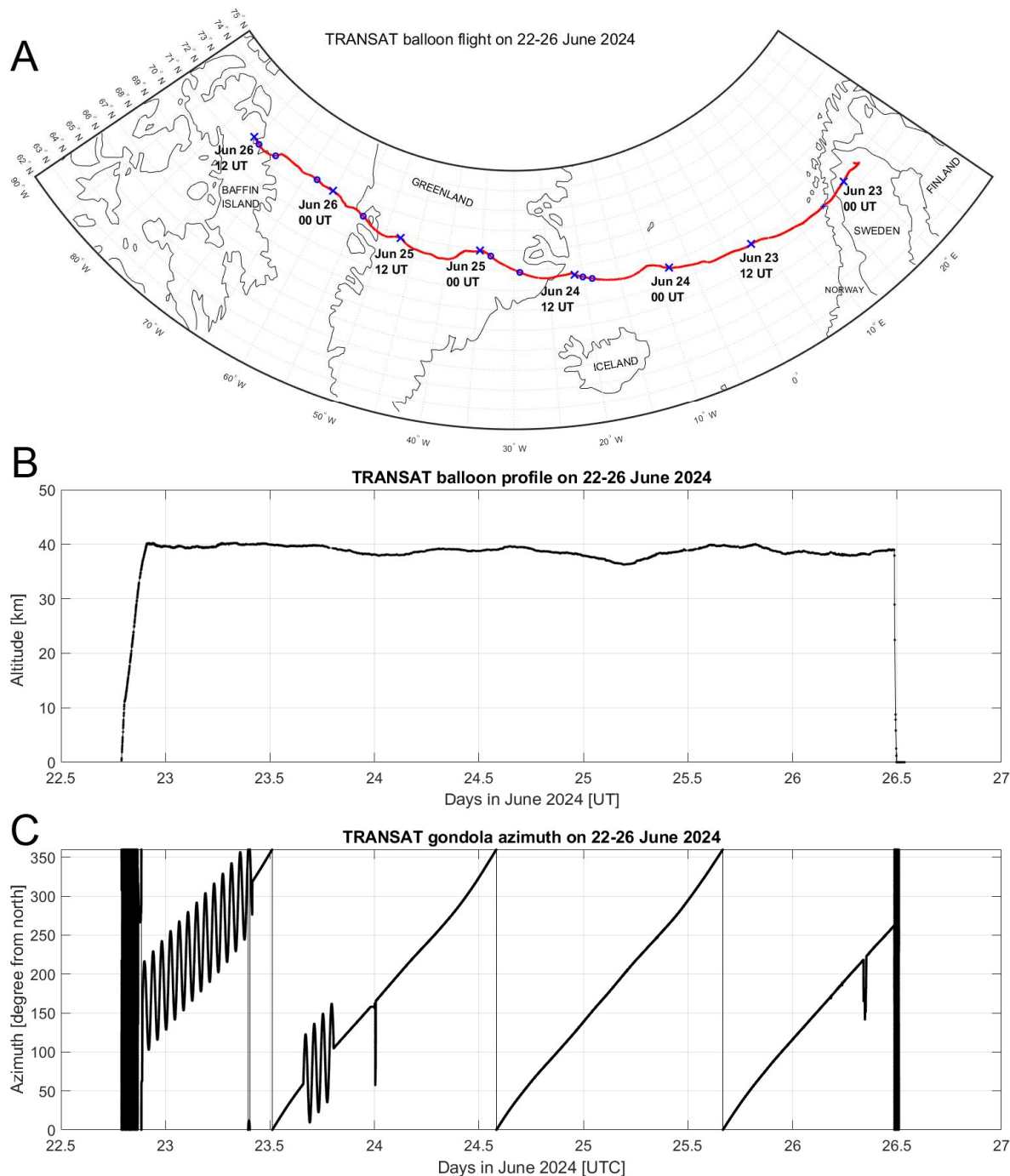
131 The Carmen gondola utilized a three-axis motorized gimbal stabilized platform, providing an elevation-angle  
132 stability of 0.15°, an absolute azimuth pointing accuracy of 1° and a stability of  $\pm 10$  arcmin around it. Because  
133 stratospheric balloons rotate continuously, such stabilization was critical to avoid image smearing and to  
134 maintain consistent NLC monitoring at fine and large scales.

135 As the transatlantic flight took place under solstice conditions with continuous solar illumination, scientific  
136 instruments were mounted behind a solar shield to prevent overheating and stray-light interference. To ensure  
137 continuous shading, the gondola was slowly rotated to keep the solar shield facing the Sun throughout the flight.

138 **Due to different scientific experiments onboard requiring different pointing directions, sometimes the**  
139 **anti-sun direction was not observed, but the oscillations around the leading azimuth of the gondola**  
140 **remained under control (see Fig. 1c). When the Sun illuminated the camera lens or strong solar reflections**  
141 **were present, such images were removed from the image analysis as overexposed. The number of the**  
142 **overexposed removed image accounted for about 2% of the total number of images analyzed.**

143 The TRANSAT balloon was launched from Esrange, northern Sweden (67.89° N, 21.08° E) at 18:57 UTC  
144 (20:57 LT) on 22 June 2024 and landed on Baffin Island, northern Canada, at 12:14 UTC (08:14 LT) on 26 June  
145 2024. The total flight time was about 90 h (3.8 days), with an average horizontal speed of about 11 m s<sup>-1</sup>. The  
146 horizontal trajectory and altitude profiles of the TRANSAT mission are shown in Fig. 2.

147



148  
 149 **Figure 2: (A) Horizontal trajectory (the red line) of the TRANSAT balloon mission between 22 and 26**  
 150 **June 2024. The blue crosses mark the balloon's position every 12 h. The blue circles show the balloon's**  
 151 **positions when no NLC were observed, see Section 4.1. (B) Altitude profile of the TRANSAT flight. (C)**  
 152 **Azimuth of the optical axis of the left camera of the SONC imager due to the TRANSAT gondola rotation**  
 153 **in the anti-sun direction for most of the flight.**

154

### 155 2.3 Image processing

156 Prior to launch, all three Sony cameras underwent geometrical calibration on the ground using night-sky  
 157 images containing reference stars. A second-order polynomial camera model was fitted by comparing theoretical  
 158 and measured horizontal coordinates for over 200 identified reference stars. Six free coefficients describing focal

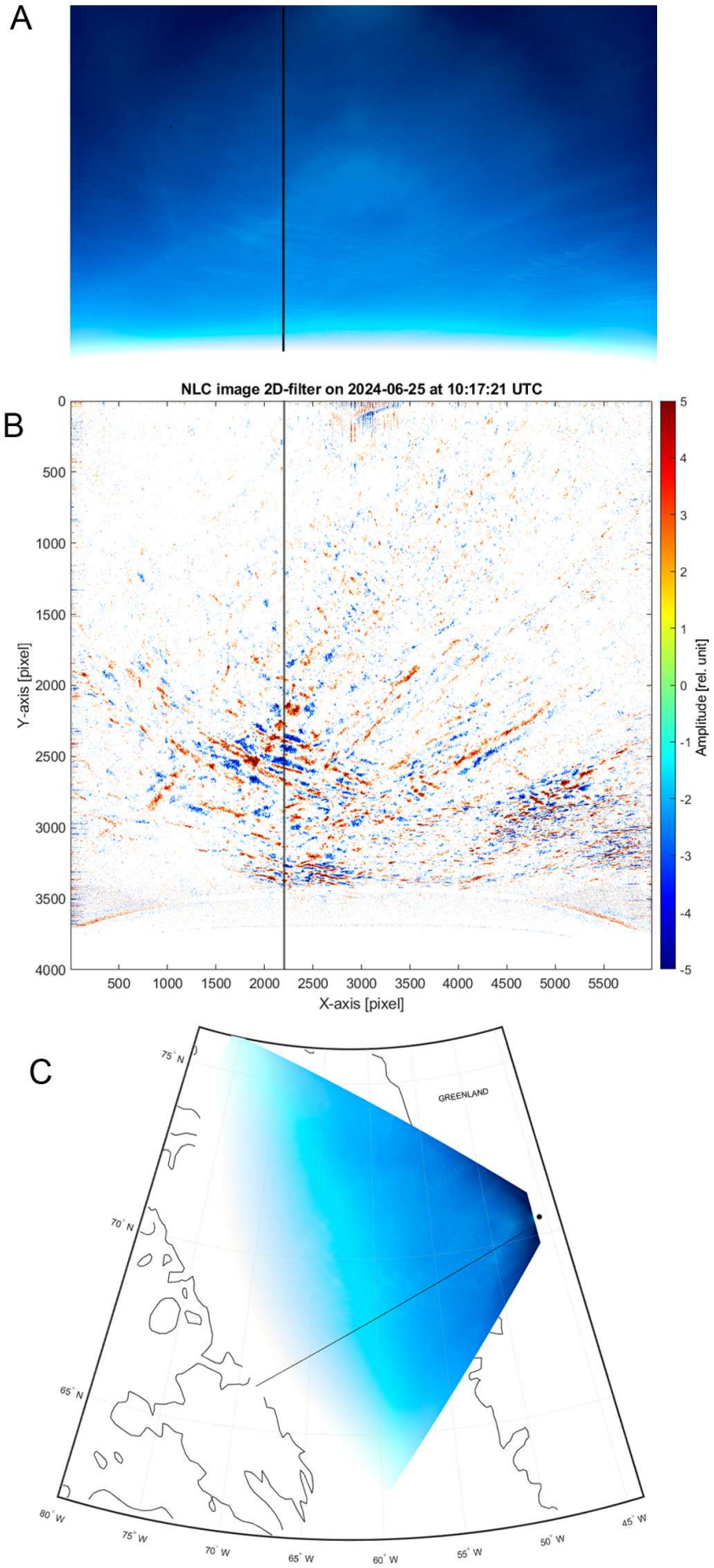
159 length, image orientation, and optical distortion were determined. These coefficients were used to compute  
 160 relative horizontal coordinates (elevation and azimuth angles relative to the center of the image) for every pixel  
 161 of each camera.

162 Given the known position and orientation of the SONC imager within the gondola reference frame, provided  
 163 by CNES, the absolute horizontal coordinates of all pixels were computed. Subsequently, a georeferencing  
 164 procedure projected each pixel onto the Earth's surface, assuming a mean NLC altitude of 83 km. Details of the  
 165 calibration, georeferencing, and error analysis are available in Dalin et al. (2015).

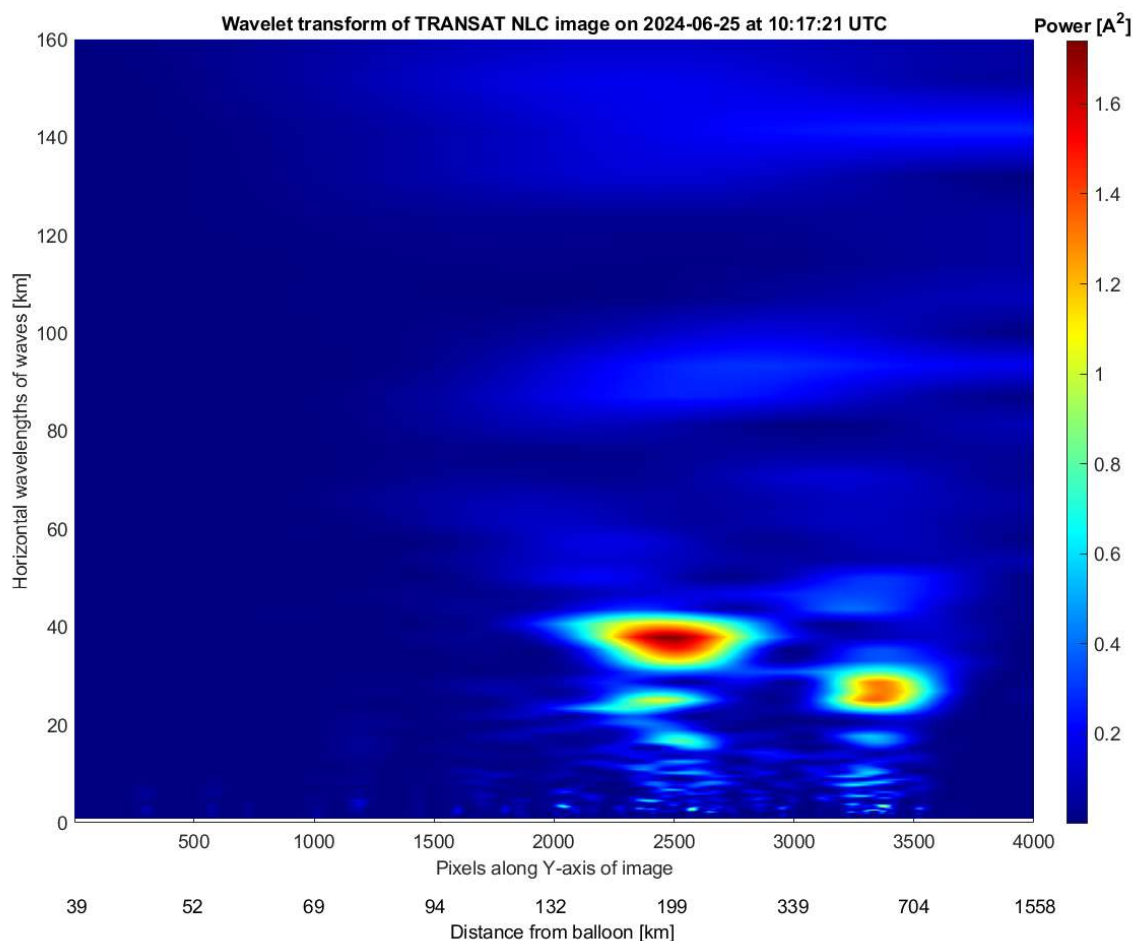
166 NLC identification was performed using both manual and automatic approaches. In the manual procedure,  
 167 about 6200 images, suitable for scientific analysis, from the left camera (Fig. 1) were carefully examined to mark  
 168 NLC presence or absence. **A separate text file was created that indicates the cloud-free times during the**  
 169 **TRANSAT flight.** The number of images is 6200 because almost every image in a series of 5 images, taken in  
 170 bracketing mode, was analyzed. A video sequence was then assembled to verify temporal continuity. This video,  
 171 containing all images with synchronized flight parameters, timestamps and balloon coordinates, is available at  
 172 the Harvard Dataverse repository (<https://doi.org/10.7910/DVN/1PHRZU>).

173 Automatic image processing involved several steps: (1) Background subtraction: a second-order polynomial  
 174 fit was used to estimate the sky background along each vertical column of pixels, which was then subtracted to  
 175 yield a residual brightness of each pixel. (2) Two-dimensional ~~Fourier~~ **digital** filtering: applied to a residual  
 176 brightness to extract gravity-wave-like patterns on image (see Fig. 3b). **To do this, we use zero-phase digital**  
 177 **filtering by processing the residual brightness in forward and reverse directions along every vertical and**  
 178 **horizontal line of the analyzed image. After filtering the data in the forward direction, the procedure**  
 179 **reverses the filtered sequence and runs it back through the filter that provides a zero-phase distortion. A**  
 180 **4th-order Butterworth bandpass filter with a lower cutoff frequency of 0.0013 Hz and a higher cutoff**  
 181 **frequency of 0.2 Hz is applied in this digital filtering procedure.** (3) Wavelet analysis: a Morse analytic  
 182 wavelet transform was applied to selected images to quantify horizontal wavelengths of identified wave patterns.  
 183 ~~Each~~ **An analyzed** image was first projected onto Earth geographical coordinates (in km) prior to **wavelet**  
 184 analysis. An example (Fig. 4) shows dominant horizontal wavelengths of about 30 and 40 km, which are  
 185 frequently observed in NLC (Pautet et al., 2011; Demissie et al., 2014). **In the present case, wave analysis was**  
 186 **applied to the vertical slice (along the Y-axis) at the constant X=2200 pixels of the filtered image shown in**  
 187 **Fig. 3b. This example was chosen at random from 6200 images, but which demonstrates the NLC**  
 188 **modulation due to gravity waves with the naked eye. Therefore, this analysis technique was applied to this**  
 189 **image in order to estimate the horizontal scales of the wave packet in this case.**

190 **The spatial horizontal resolution of the pixels in the upper part of the projected image (close to the**  
 191 **balloon) is about 21 m, of the pixels in the middle of the image is about 96 m, and of the pixels at the**  
 192 **bottom of the projected image is about 1.2 km. In accordance with the Nyquist–Shannon sampling**  
 193 **theorem, these values allow the study of NLC signals with horizontal scales greater than 42 m, 192 m and**  
 194 **2.4 km, respectively. Thus, medium- and large-scale gravity waves with horizontal wavelengths greater 50**  
 195 **km, small-scale gravity waves of 10-50 km, smaller-scale localized waves (billows or ripples) of 3-10 km**  
 196 **can be analyzed throughout the image. Also, turbulent structures like vortex rings of 0.5-4 km in diameter**  
 197 **can be studied in the upper and middle part of the image (Dalin et al., 2010; Pautet et al., 2011;**  
 198 **Baumgarten and Fritts, 2014; Fritts et al., 2017; Fritts et al., 2019).**



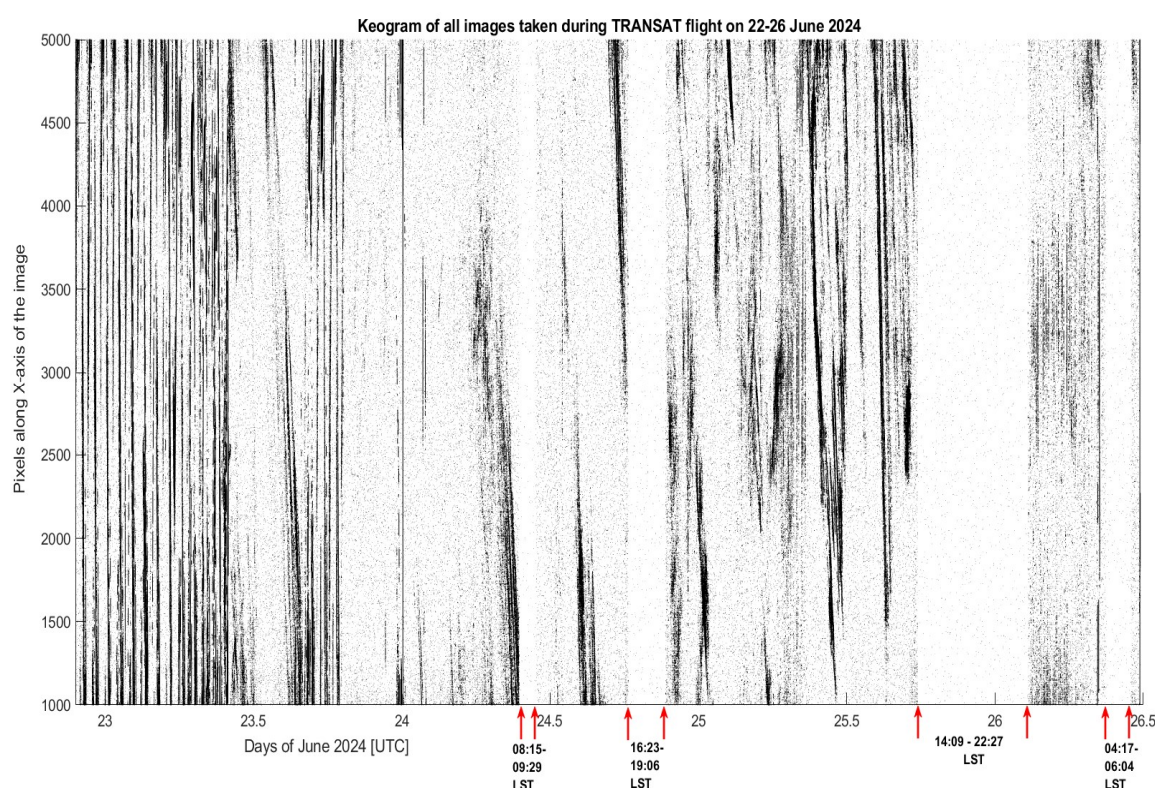
200 **Figure 3: (A) Example of NLC image acquired at 10:17:21 UTC on 25 June 2024 during the TRANSAT**  
 201 **balloon flight. (B) Two-dimensional Fourier-filtered version of (A), highlighting residual brightness**  
 202 **variations associated with NLC bands seen in the middle and the lower part of the image. (C) Projection**  
 203 **of the NLC image shown on panel A onto the Earth's surface. The black dot is the position of the**  
 204 **TRANSAT balloon. The black line shown in panels A, B and C shows the vertical slice at X=2200 pixels**  
 205 **where wavelet analysis was applied (see the text).**



206 **Figure 4: Example of a wavelet transform for the NLC image obtained at 10:17:21 UTC on 25 June 2024**  
 207 **during the TRANSAT flight. Gravity waves having prevailing horizontal scales of about 30 and 40 km are**  
 208 **clearly seen as the red color code. Two different scales on the X-axis are present: the upper scale is in**  
 209 **pixels along the Y-axis at X=2200 pixels of the image shown in Fig. 3a, the lower scale is the distance from**  
 210 **the TRANSAT balloon in km.**

212  
 213 4) A keogram representation of a sequence of all analyzed images helps to identify the presence or absence of  
 214 NLC as a function of time. A keogram is a slice of an image along a specific axis, and many such slices are put  
 215 together as a function of time to produce brightness variations of an observed atmospheric phenomenon over  
 216 time. A keogram is commonly used to demonstrate a presence or absence of aurora in all-sky images. In the  
 217 present study, based on the manual careful inspection of 6200 images suitable for scientific analysis, we have  
 218 selected horizontal pixel lines in the range of 3000-3400 pixels (counting along the Y-axis from the top of the  
 219 image) at which NLC preferred to appear. **These pixels correspond to a distance of about 315-583 km from**

220 **the gondola position, when looking along the central line of the image.** The image coordinates are present in  
 221 Fig. 3b. These pixels were summed to produce an integrated brightness for every column between 3000 and  
 222 3400 pixels. The mean value and its standard deviation (std) were then calculated for the given slice along the X-  
 223 axis of the image. **We have separately estimated the mean brightness and its standard deviation for each**  
 224 **image, thus the obtained values are independent of time and camera azimuth.** Next, a selection rule was  
 225 applied: brightness values greater than 1 std of the mean were selected to classify the given slice as NLC present  
 226 or absent. Then **the** keogram was created by putting together slices of about 6200 images (Fig. 5), demonstrating  
 227 nearly continuous presence of NLC, that is discussed in detail in Section 4. This automatic keogram procedure  
 228 fits well with the manual procedure (described above) in identifying the presence or absence of NLC as a  
 229 function of time. **The time intervals of the absence of NLC are indicated by red arrows that coincide with**  
 230 **the manual and automatic procedure.**



231  
 232 **Figure 5: Keogram compiled from about 6200 images during the TRANSAT balloon flight on 22-26 June**  
 233 **2024. The red arrows mark four time intervals (white-grey areas) when NLC were absent. Corresponding**  
 234 **local solar times (LST) are shown for four time intervals on the x-axis. LST are calculated for the gondola**  
 235 **position, but not for the observed NLC. The number of Y-pixels is equal to 401 for which the keogram was**  
 236 **constructed.**

### 237

## 238 3 Ground-based and space complementary measurements

### 239 3.1 Lidar measurements

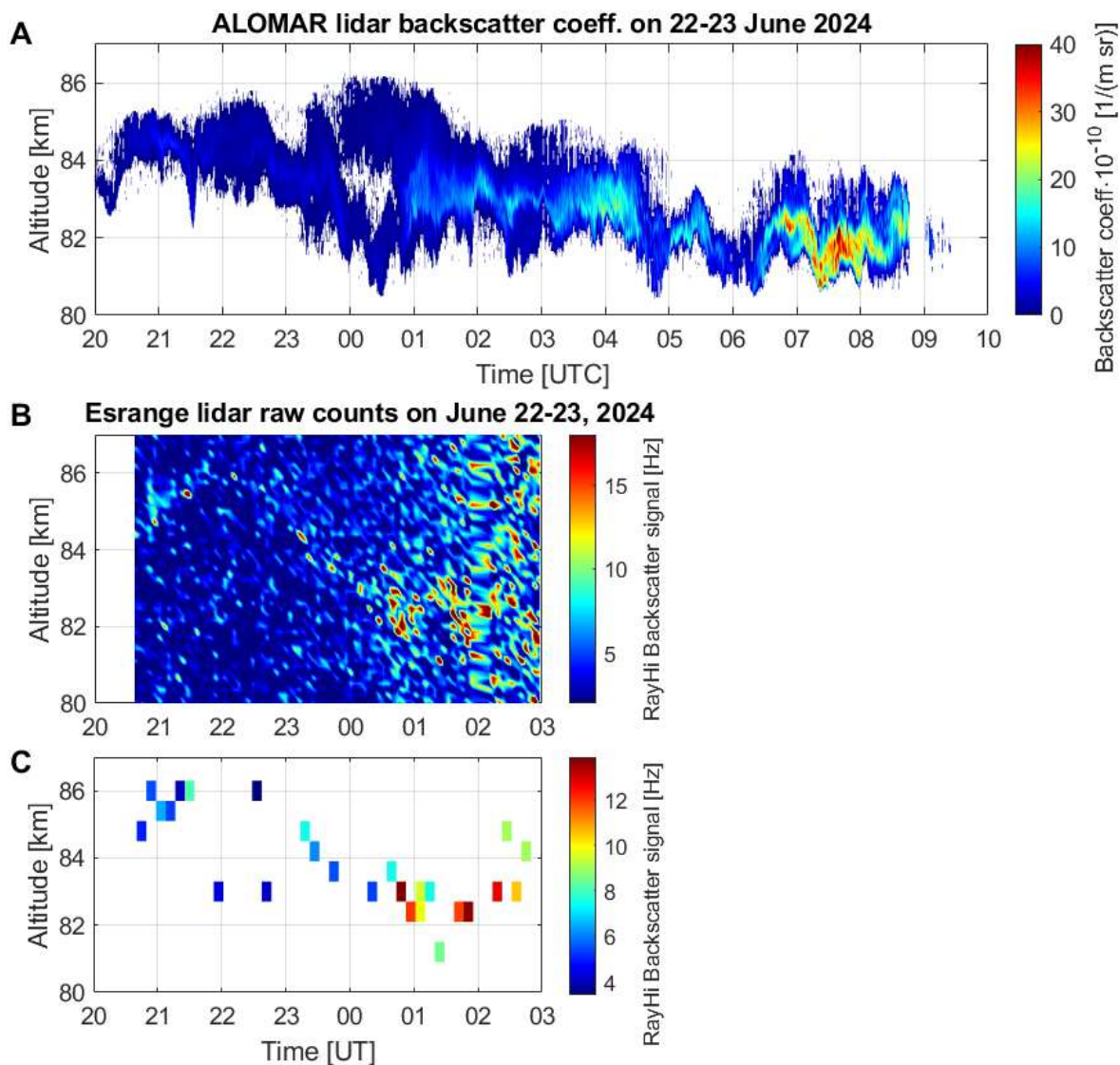
240 During the initial phase of the TRANSAT balloon flight, complementary lidar measurements were  
 241 performed at Esrang (67.8°N, 21.1°E, Sweden) and Andøya (69.3°N, 16.0°E, Norway), with the aim to provide  
 242 simultaneous and common volume (or in proximity) measurements of NLC layers above northern Scandinavia.

243 At Esrange, we use a Rayleigh/Mie/Raman (RMR) backscatter lidar developed by the Bonn University to  
 244 monitor aerosols in the troposphere, stratosphere and mesosphere as well as to determine temperature profiles in  
 245 the aerosol-free part of the atmosphere (Blum and Fricke, 2005). The vertical and time resolution of the obtained  
 246 measurements by the Esrange lidar is 150 m and 4.4 min, respectively. At Andøya, we use an RMR-lidar which  
 247 has been operated as part of the Arctic Lidar Observatory for Middle Atmosphere Research (ALOMAR). Using  
 248 measurements of the ALOMAR lidar one can study temperatures and winds in the middle atmosphere, aerosol  
 249 layers in the stratosphere, polar stratospheric clouds in the lower stratosphere in winter and noctilucent clouds in  
 250 the mesopause region in summer (Baumgarten, 2010). We use lidars backscattered signals from the 532-nm  
 251 wavelength channel to measure NLC over Esrange and Andøya during the TRANSAT flight **in the stratosphere**  
 252 over northern Scandinavia. The vertical and time resolution of the obtained measurements by the ALOMAR  
 253 lidar is 40 m and 30 s, respectively.

254 **The results of the lidar measurements during the initial phase of the TRANSAT flight are shown in**  
 255 **Fig. 6. The NLC layer is clearly seen in both lidar measurements between 81 and 86 km altitude from**  
 256 **20:30 UTC on 22 June until 01:00 UTC on 23 June. Figure 6b shows raw Esrange lidar counts and Fig. 6c**  
 257 **represents the filtered lidar data in the following way. All Esrange lidar data were averaged over a 600 m**  
 258 **altitude interval and a 9-minute time interval. Then the atmospheric background was estimated as the**  
 259 **average value, and its standard deviation, of the lidar raw counts between 80 and 87 km for each time-**  
 260 **averaged measurement. Counts exceeding 1.5 standard deviations from the average value were then**  
 261 **selected. Figure 6c highlights the main features of the NLC layer seen in Fig. 6b.** Between 20 and 22 UTC,  
 262 the NLC layer lifted up from 84 to 86 km, then it sank to ~~81~~ **about** 82 km between 22 UTC on 22 June and 01  
 263 UTC on 23 June as demonstrated by both lidars. **After 01 UTC, Esrange lidar measurements become too**  
 264 **noisy to distinguish the NLC signal from noise.** Note that the ALOMAR lidar registered a double-layer NLC  
 265 structure between 00 and 01 UTC. Another double-layer NLC structure will be discussed in section 4. These  
 266 height variations of the NLC layer are due to propagating atmospheric gravity waves ~~and turbulent vorticities~~.  
 267 Note that it is a very rare case of conducting simultaneous lidar measurements at Andøya and Esrange (separated  
 268 by ~250 km) on both sides of the Scandinavian range, registering about the same NLC layer. ~~After 01 UTC,~~  
 269 ~~Esrange lidar measurements become too noisy to distinguish the NLC signal from noise.~~ The ALOMAR lidar  
 270 operated until 12 UTC on 23 June, continuously registering the enhanced NLC layer until **about 09:30** UTC,  
 271 with height variations between 81 and 84 km. The extended NLC field was registered **by the SONC imager**  
 272 **from the stratosphere** above northern Scandinavia (not shown in figure) ~~shortly after the TRANSAT balloon~~  
 273 ~~launch~~ **starting from ~22 UTC on 22 June 2024** and during the lidar measurements, thus continuously observing  
 274 nearly the same NLC layer from the ground and stratosphere from evening hours on 22 June until morning hours  
 275 on 23 June.

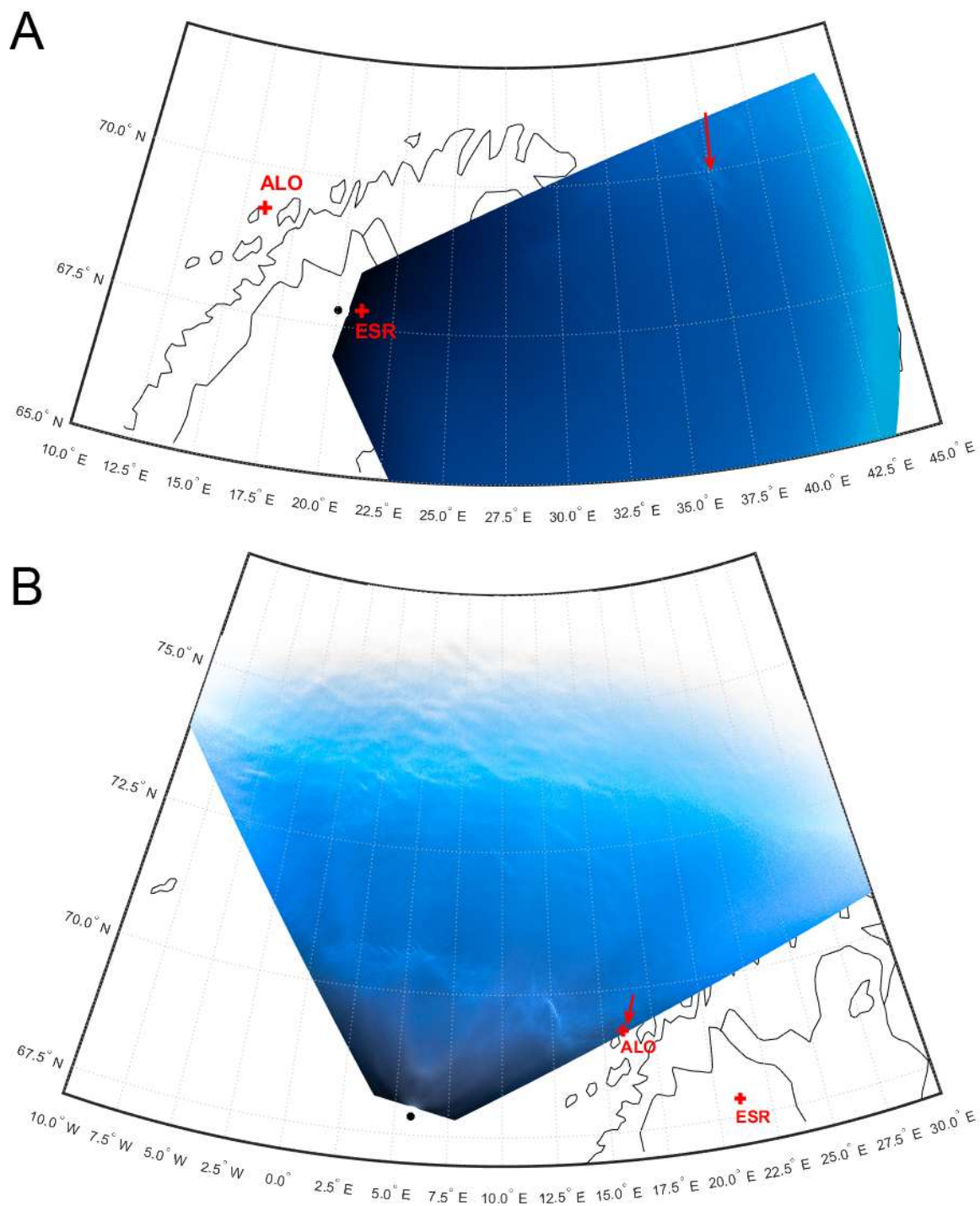
276

277



278  
 279 **Figure 6: Lidar measurements at Andøya, Norway (upper panel A) and Esrange, Sweden (lower panel B)**  
 280 **during the initial phase of the TRANSAT balloon flight on 22-23 June 2024. (C) Filtered Esrange lidar**  
 281 **data averaged over a 600 m altitude interval and a 9-minute time interval (see the text).**

282  
 283 **Figure 7 illustrates the SONC images at 22:04:38 UTC on 22 June and at 09:34:32 UTC on 23 June,**  
 284 **i.e., at the beginning and end of the NLC observations by the Esrange and ALOMAR lidars. At the**  
 285 **beginning of the lidars measurements the NLC observed by the SONC imager were located to the east of**  
 286 **the lidars, but at the same latitude range (Fig. 7a). Later, the SONC imager slowly rotated in the antisolar**  
 287 **direction, observing the east-south-west sector of the sky, and, thus, observations of NLC in the**  
 288 **mesopause over the lidars were impossible. At the same time, at the very end of the ALOMAR lidar**  
 289 **observations at about 09:30 UTC on 23 June, the SONC imager looked north-northeast and detected faint**  
 290 **NLC at the very edge of the image frame directly over the ALOMAR lidar (Fig. 7b). At that time, NLC**  
 291 **were between 81.6 and 82.0 km (Fig. 6a).** Thus, lidar measurements complement balloon-borne observations,  
 292 providing information on vertical dynamics of the NLC layer observed from the stratosphere.



293  
 294 **Figure 7: Projection of two SONC images on the Earth's surface at 22:04:38 UTC on 22 June 2024 (A)**  
 295 **and at 09:34:32 UTC on 23 June 2024 (B) during the TRANSAT balloon flight. The black dot denotes the**  
 296 **balloon position. The red crosses are the position of the ALOMAR (ALO) and Esrange (ESR) lidars. The**  
 297 **red arrows show the locations of NLC.**

298

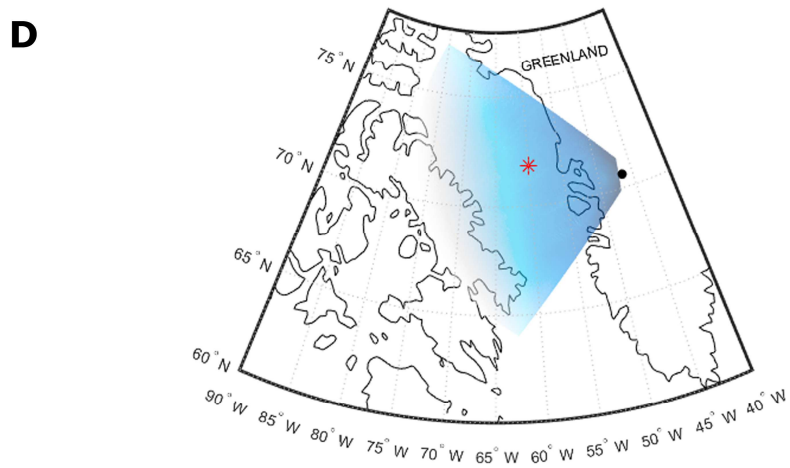
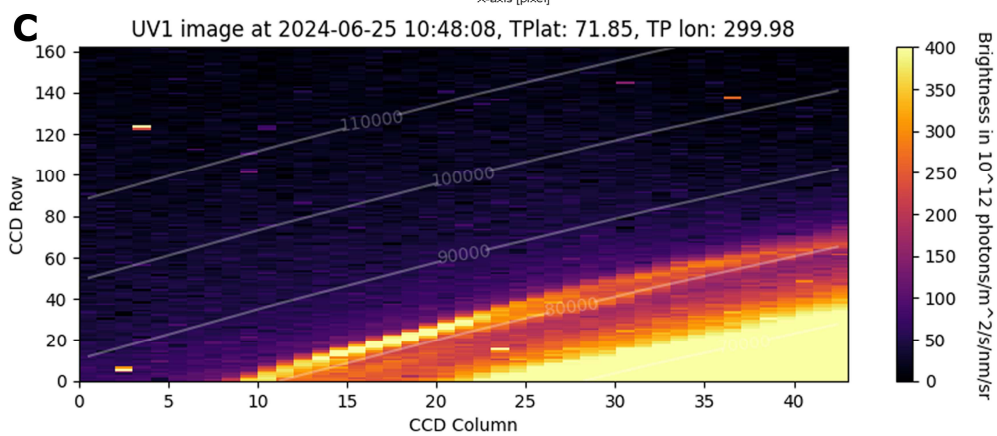
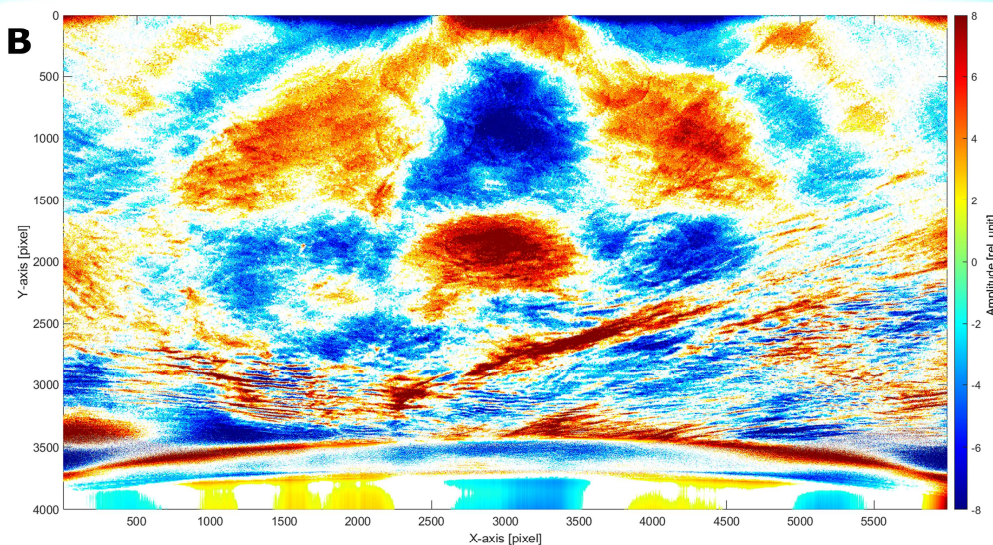
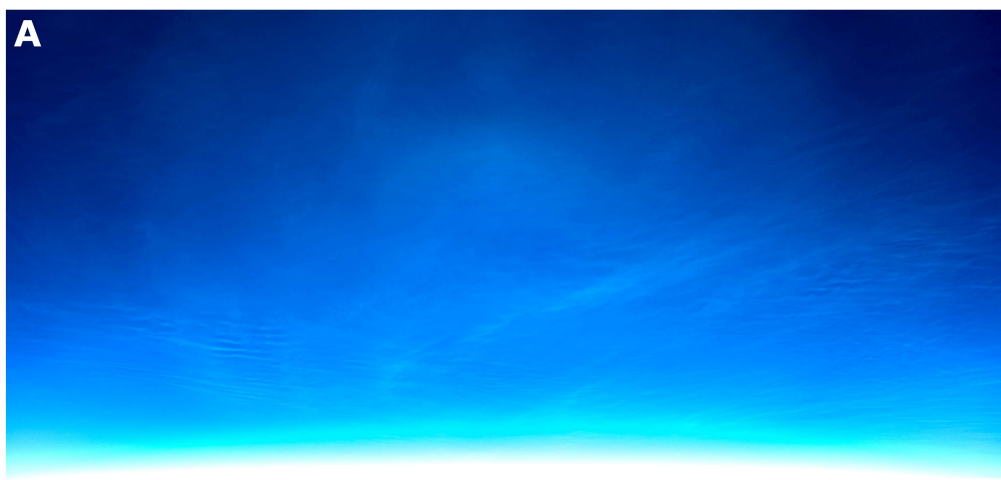
299

### 3.2 Space measurements

300 During the TRANSAT flight, measurements of PMC from space were also conducted with the MATS  
 301 satellite. MATS (Mesospheric Airglow/Aerosol Tomography and Spectroscopy) is a Swedish satellite mission,  
 302 launched in November 2022, designed to investigate polar mesospheric clouds, temperature regime and  
 303 atmospheric gravity waves in the mesosphere (Gumbel et al., 2020). The MATS satellite utilizes airglow  
 304 emissions coming from excited molecular oxygen in the near infrared range of the spectrum (760-780 nm, the O<sub>2</sub>  
 305 (0-0) A-band) as well as scattered light from PMC in the ultraviolet (270 and 340 nm). The primary scientific  
 306 instrument on-board the satellite is the limb imager, a telescope with ~~6~~ **six** wavelength channels that continuously  
 307 captures **high-resolution** images of the atmospheric limb with a field of view of about 40 km in the vertical and  
 308 250 km across track at the tangent point. **The horizontal and vertical resolution of MATS limb images is 5.7**  
 309 **km and 290 m, respectively. The horizontal resolution is consistent with AIM/CIPS images (Randall et al.,**  
 310 **2017) and the vertical resolution of 290 m should be considered high for satellite missions.** Using a  
 311 tomographic analysis of acquired MATS images, one can reconstruct waves in three dimensions and provide 3-  
 312 dimensional fields of airglow, PMC properties and temperature (Megner et al., 2025).

313 Figure 7 **8** demonstrates an example of MATS images in the UV channel 1 at 270 nm taken at 10:48:08 UTC  
 314 on 25 June 2024. This measurement was done at the tangent point in the mesopause close to the west coast of  
 315 Greenland as illustrated in Fig. 7e **8d**. One can clearly see the presence of the PMC layer in Fig. 7b **8c** as the  
 316 bright yellow band on the atmospheric limb between 80 and 85 km tangent altitude. The time and location of the  
 317 PMC by MATS agree very well (time difference of 6 seconds) with the NLC observation obtained from the  
 318 **TRANSAT balloon stratosphere**, with the MATS tangent point being in the field of view of the SONC imager  
 319 as seen in Fig. 7e **8d**. Such simultaneous common-volume observation of NLC from the stratosphere and space  
 320 was made for the second time; the first one was made by the PMC Turbo stratospheric flight and the AIM  
 321 satellite in July 2018 (Fritts et al., 2019). But in the present study this was done for the first time when such a  
 322 large-scale NLC/PMC field (extending at least 1500 km from north to south) was seen from the stratosphere and  
 323 from space based on the limb-viewing observation using the MATS satellite. ~~It should also be noted that MATS~~  
 324 ~~registered the PMC layer before and after the time shown in Fig. 7, i.e.,~~ **Note that MATS also detected NLC in**  
 325 **the next orbit over Greenland and in field of view of the SONC imager at 12:22:16 UTC on June 23 (not**  
 326 **shown in figure). In the present study, we do not aim to completely compare all possible NLC observations**  
 327 **from the stratosphere and the MATS satellite, but to demonstrate the fundamental possibility of such**  
 328 **observations in one figure only. Thus,** MATS observed an extended PMC layer in a large volume of the  
 329 mesopause at least over Greenland, Baffin Bay and Baffin Island. Part of this large-scale NLC field was  
 330 registered from the stratosphere by the SONC imager **shown in Fig. 8a. Figure 8b demonstrates a 2D-filtered**  
 331 **image with a second-order polynomial removed from the original image (see section 2.3), which shows**  
 332 **NLC modulations due to gravity waves of various scales throughout the lower part of the image.** At the  
 333 same time, images taken from the stratosphere have much higher spatial resolution, showing small- and medium-  
 334 scale wave dynamics (including smaller gravity waves and turbulent structures) that MATS cannot resolve using  
 335 the limb-viewing geometry. Thus, studies of spatial-temporal variability of NLC/PMC can be carried out  
 336 simultaneously from the stratosphere and space, complementing each other.

337



339 **Figure 7 8: Example of NLC measurements obtained from the stratosphere and space on 25 June 2024**  
 340 **during the TRANSAT balloon flight. (A) Image, taken by the SONC imager from the stratosphere at**  
 341 **10:48:02 UTC, shows the extended NLC field covering almost the whole image area. (B) 2D-filtered image**  
 342 **with a second-order polynomial removed from the original image shown in A (see the text). (B C) Image,**  
 343 **taken by the MATS satellite at 10:48:08 UTC, illustrate part of the atmospheric limb, with the bright**  
 344 **yellow PMC layer seen between 80 and 85 km. Data are shown for the UV channel 1 at 270 nm. (C D)**  
 345 **Projection of the NLC image shown on Panel A onto the Earth's surface. The black dot is the position of**  
 346 **the TRANSAT balloon, the red asterisk marks the MATS tangent point which is in the field of view of the**  
 347 **SONC imager.**

348

## 349 4 Results and Discussion

### 350 4.1 Nearly continuous observations of NLC

351 The first unexpected scientific result is the nearly continuous presence of mesospheric clouds **in the**  
 352 **observed latitude range of 60–75°N** during 3.8 days of the TRANSAT balloon flight. In total, there were four  
 353 intervals of NLC disappearances as shown **by the blue circles in Fig. 2a and** by the red arrows in Fig. 5. These  
 354 events occurred on 23 June at 09:30–10:50 UTC on 23 June, at 18:20–21:20 UTC on 24 June, at 17:45–02:40  
 355 UTC on 25-26 June, and at 09:00–11:00 UTC on 26 June. Outside these intervals, NLC were continuously  
 356 observed, often with varying brightness and wave modulation.

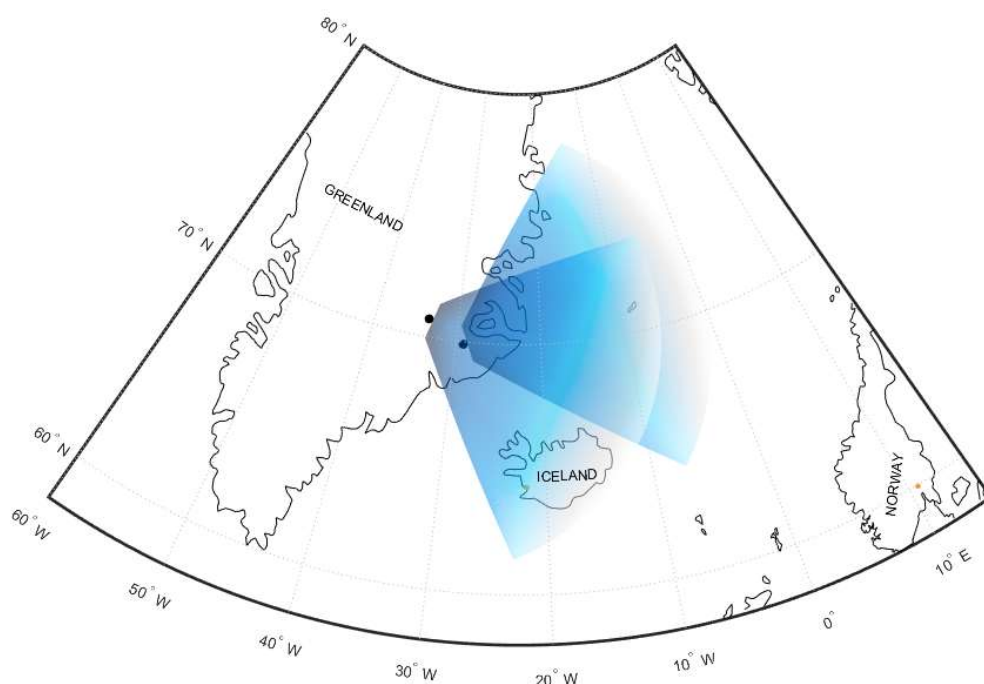
357 These NLC disappearances are not related to local solar time (see four local solar time intervals on the x-axis  
 358 in Fig. 5). That is, these NLC interruptions were of a rather spontaneous nature and were not related to solar  
 359 thermal tides, which are regular atmospheric variations. Indeed, Fritts et al. (2019) demonstrated more or less  
 360 regular NLC disappearances in the evening (18-24 LST) and morning hours (6-12 LST), observed during the  
 361 PMC Turbo balloon flight from Sweden to Canada in July 2018. The authors associated this with solar  
 362 semidiurnal and diurnal thermal tides in the polar summer mesopause, the amplitudes of which reach 10-20 K,  
 363 which is comparable to ones by gravity waves in the mesopause region (Rapp et al., 2002). It should be noted  
 364 that this result was obtained on the basis of lidar measurements on the PMC Turbo balloon, that is, obtained with  
 365 a very small field of view of a few meters in the mesopause. Therefore, for such a small volume of the  
 366 mesopause one can expect the dominant influence of large-scale waves such as solar tides. **Note that continuous**  
 367 **lidar observations at 69°N demonstrate strong NLC diurnal variations due to solar tides, with a maximum**  
 368 **occurrence frequency of about 65% in the morning hours and a minimum of about 35% around noon**  
 369 **(Fiedler et al., 2011).** In the case of the TRANSAT balloon flight NLC observations were carried out on large  
 370 scales of about 1000-1500 km at a time. At such large scales, not only solar tides manifest themselves but also  
 371 propagating gravity waves of various scales from 1 to 1000 km. Indeed, a typical picture seen from the  
 372 stratosphere was that we saw a disappearance of NLC in one area of the mesopause (for example, in the eastern  
 373 part), but simultaneous appearance of other NLC in another part of the mesopause (for example, in the western  
 374 part). In other words, large-scale NLC fields were generally represented by numerous wavy patterns of sporadic  
 375 nature. One can assume that gravity waves, continuously coming from the lower atmosphere, form a new NLC  
 376 and/or modulate an existing NLC layer in different parts of the mesopause (as observed in the present  
 377 experiment), thereby dominating solar thermal tides on large scales. At the same time, we should note that this  
 378 result was obtained on the basis of a single 3.8-day flight and a limited range of latitudes (60-75°N) and

379 longitudes (45°E-95°W). That is why the present case study cannot claim to be a general statement about the  
 380 relative importance of solar tides compared to gravity waves.

381

#### 382 4.2 A case study of the NLC disappearance

383 The second result is connected to the disappearance of NLC at 18:20-21:20 UTC (16:23-19:06 LST) on 24  
 384 June 2024 (Fig. 5). This NLC disappearance was observed over the Atlantic Ocean near the east coast of  
 385 Greenland and over Iceland as demonstrated in Fig. 8 9.



386  
 387 **Figure 8 9: Projection of the field of view of the SONC camera on the Earth's surface at 18:20 UTC (16:23**  
 388 **LST) and 21:20 UTC (19:06 LST) on 24 June 2024, when no NLC were observed from the stratosphere.**  
 389 **The black dots mark the position of the TRANSAT balloon.**

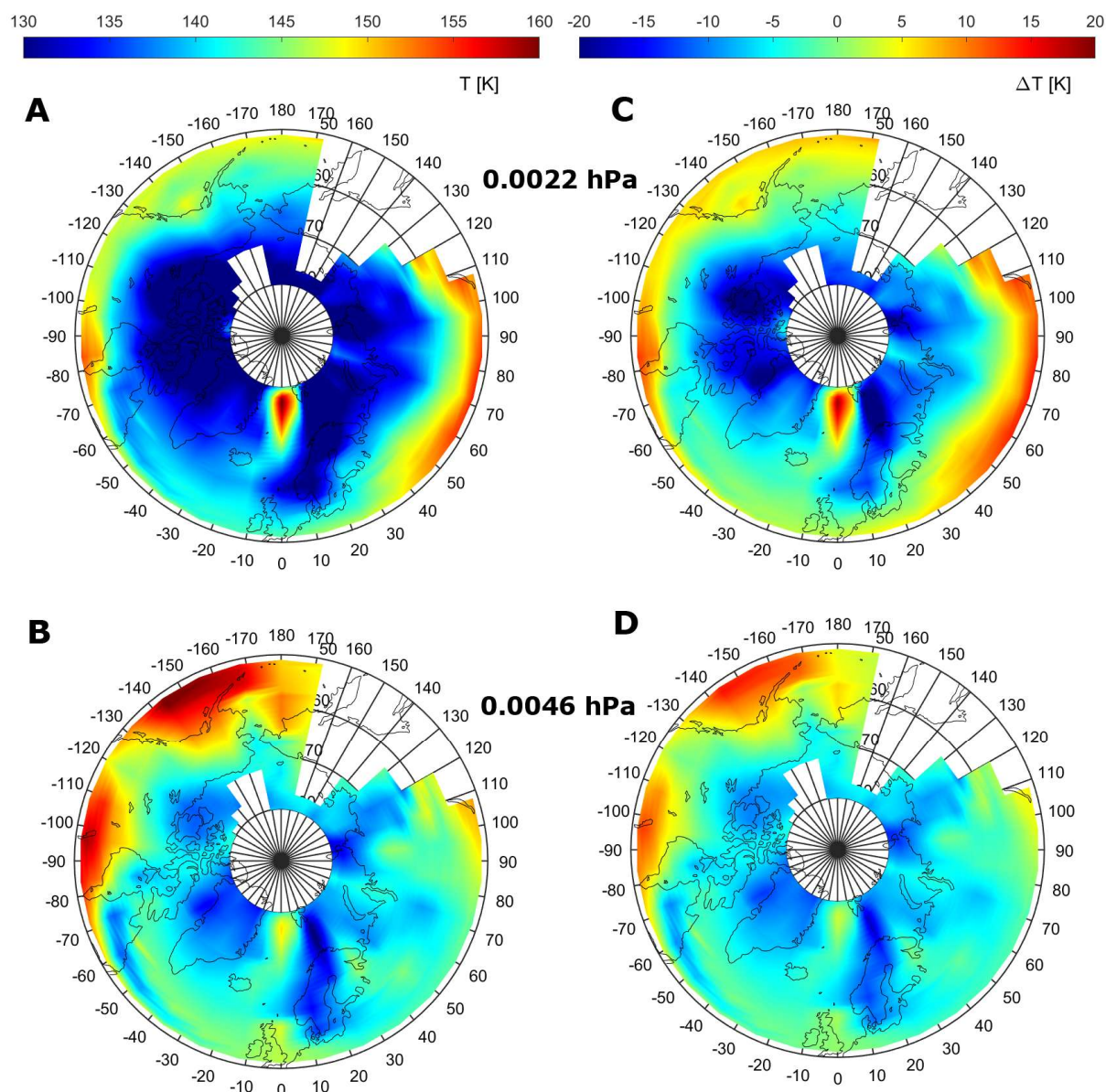
390

391 We have tried to find out the reason for this NLC disappearance. For this data of the Aura/MLS temperature  
 392 and water vapor measurements have been used to obtain a comprehensive picture of the mesopause environment  
 393 in the region of interest. Aura/MLS temperature and water vapor measurements of ver.5.0 and level 2 data  
 394 quality were obtained from the NASA public web-site:

395 [https://acdisc.gesdisc.eosdis.nasa.gov/data/Aura\\_MLS\\_Level2/](https://acdisc.gesdisc.eosdis.nasa.gov/data/Aura_MLS_Level2/). According to the Aura/MLS data quality and  
 396 description document (version 5.0x level 2 and 3), for Aura/MLS temperature measurements, the vertical  
 397 resolution in the mesopause region is 11 km at 0.01 hPa (~80 km) and 12 km at 0.001 hPa (~90 km). The

398 horizontal resolution (along track) is ~250 km at 0.01 hPa and ~280 km at 0.001 hPa. The pressure range  
399 recommended for scientific use is from 261 hPa (~10 km) to 0.00046 hPa (~93 km). Typical precisions for  
400 individual Aura/MLS temperature profiles at this altitude range are  $\pm 3.4$ – $3.6$  K. For Aura/MLS water vapor  
401 measurements, the vertical resolution is 8.8 km at 0.01 hPa and 10.3 km at 0.002 hPa. The horizontal resolution  
402 is ~725 km at 0.01 hPa and ~350 km at 0.002 hPa. The pressure range recommended for scientific use is from  
403 316 hPa to 0.001 hPa. Typical precisions for individual Aura/MLS water vapor profiles are 55% at 0.01 hPa and  
404 450% at 0.001 hPa. The description on the MLS temperature product and its validation can be found in  
405 Froidevaux et al. (2006) and Schwartz et al. (2008). The validation of water vapor data is described in detail by  
406 Read et al. (2007) and Lambert et al. (2007). The frost point temperature in the mesopause was calculated using  
407 Aura/MLS water vapor data based on thermodynamics of the vapor pressure of ice (Murphy and Koop, 2005).

408 The results are shown in Fig. 9 **10** demonstrating the following peculiar feature. A prominent localized warm  
409 area in the mesopause region at the pressure levels of 0.0022 hPa (about 86 km geometrical height) and 0.0046  
410 hPa (about 83 km) was present between Greenland and Scandinavia, with temperatures 20-30 K higher than  
411 those in the adjacent mesopause regions at 0.0022 hPa. The location of this warm spot coincides well with the  
412 position of the mesopause visible from the TRANSAT balloon when no NLC were seen (Fig. 8 **9**). The right  
413 column in Fig. 9 **10** shows the differences between the actual temperature measurements and the frost point  
414 temperature as calculated using Aura/MLS water vapor measurements, with positive temperature differences  
415 being as much as 10-15 K in the center of this warm spot. We double-checked all the Aura/MLS data  
416 (temperature and water vapor) which show good quality data suitable for scientific analysis and we could not  
417 find any error in these data.



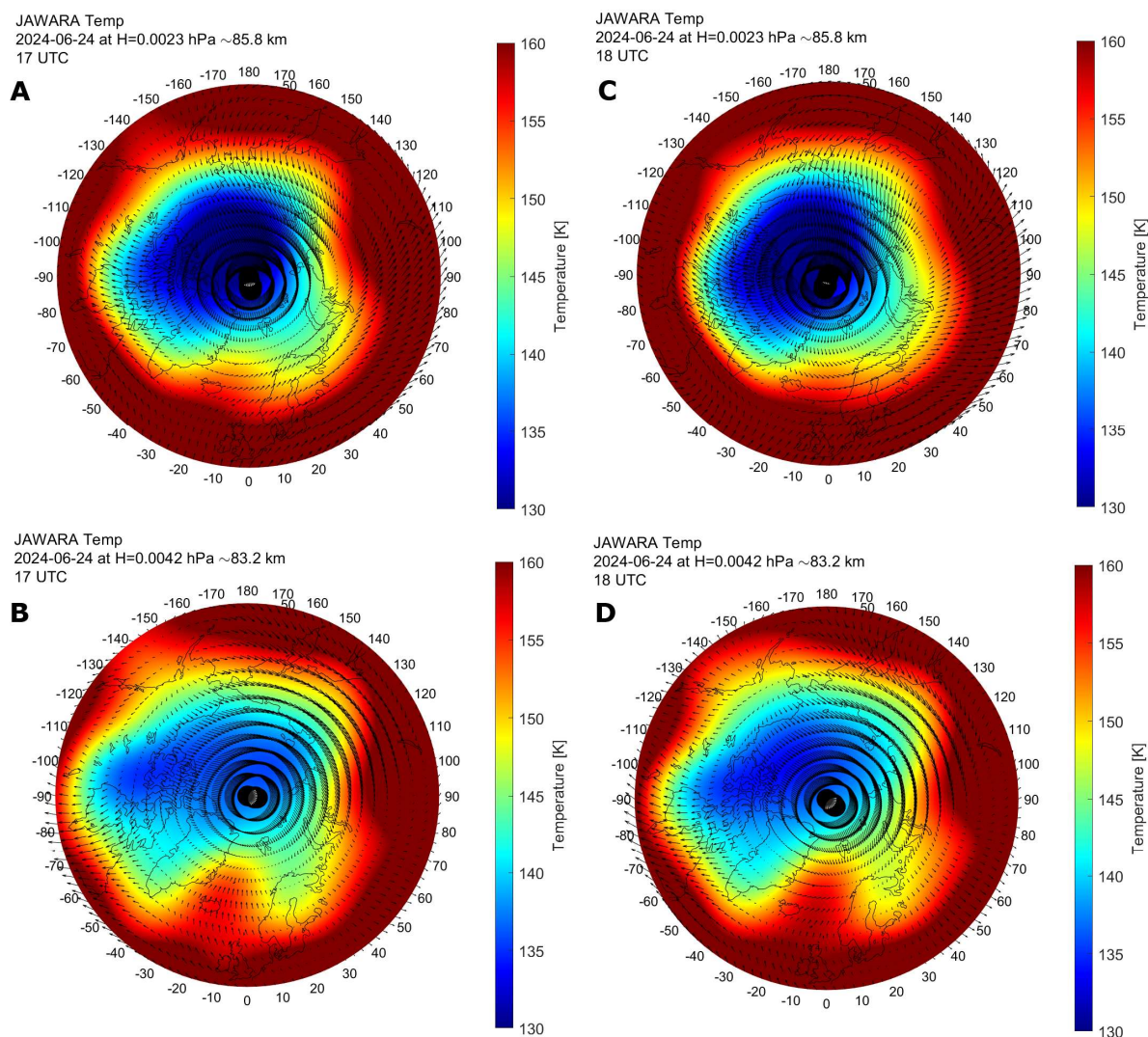
418  
 419 **Figure 9 10:** (Left column **A**) Aura/MLS temperature measurements at the pressure level of 0.0022 hPa  
 420 (~86 km) and **(B)** at 0.0046 hPa (~83 km) on 24 June 2024. (Right column) Differences between the  
 421 temperature and the frost point temperature as estimated based on Aura/MLS water vapor measurements  
 422 at 0.0022 hPa **(C)** and 0.0046 hPa **(D)**, see the text.

423  
 424 In Fig. 9 10 (especially in plots for the 0.0046 hPa level), one can note that the warm local region at high  
 425 latitudes was an extension of a warm vast area located at mid-latitudes. That is, one can assume that this local  
 426 warm region was caused by a jet of warm air mass from middle latitudes to high latitudes. To test this  
 427 hypothesis, we apply the Japanese Atmospheric General circulation model for Upper Atmosphere Research Data  
 428 Assimilation System (JAGUAR-DAS), which is a data assimilation system for the whole neutral atmosphere  
 429 (Koshin et al., 2020; 2022). Specifically, JAGUAR-DAS Whole neutral Atmosphere Reanalysis (JAWARA) has  
 430 been considered in the present study. JAWARA is a long-period reanalysis, starting from September 2004,  
 431 which covers the altitude range from the surface to the lower thermosphere (~110 km). The vertical resolution of  
 432 JAWARA data in the mesopause region between 80 and 90 km is about 0.7 km. JAWARA outputs, distributed

433 on a horizontal grid spacing of  $2.81^\circ$ , include the following hourly data: temperature, zonal, meridional and  
 434 vertical wind velocities, geopotential height, temperature tendency due to diabatic heating, zonal and meridional  
 435 forcing from the GW parameterization (Koshin et al., 2025). Note that JAWARA assimilates MLS temperature,  
 436 meaning that the temperature fields in MLS and JAWARA are not fully independent and the mutual agreement  
 437 might be expected because of the data assimilation.

438 JAWARA temperature and neutral wind data in the mesopause region are shown on 24 June 2024 in Fig. 10  
 439 11, demonstrating the following features. The warm localized spot was present between Greenland and  
 440 Scandinavia, and it was most pronounced at 0.0042 hPa,  $\sim 83$  km, (lower plots), which agrees well with the  
 441 position of the warm spot represented by Aura/MLS. At the same time, wind velocity vectors show that the local  
 442 wind jet was formed, which moved from middle to high latitudes in the region with this warm spot. Thus, this  
 443 warm spot in the mesopause was caused by the intrusion of a warm air mass from the middle to high latitudes  
 444 between Greenland and Scandinavia. This warm spot induced sublimation of ice particles in the mesopause,  
 445 which caused NLC to disappear during the TRANSAT balloon flight over the North Atlantic and the east coast  
 446 of Greenland in the evening of 24 June 2024. The mechanism of this air intrusion from middle to high latitudes  
 447 is beyond the scope of the present paper.

448



449

450 **Figure 11: JAWARA model temperature (color code) and neutral wind velocity vectors (arrows) on 24**  
 451 **June 2024. The data are shown at the pressure level of 0.0023 hPa (upper panels A and C) and at 0.0042**  
 452 **hPa (lower panels B and D), and at 17:00 UTC (left column A and B) and at 18:00 UTC (right column C**  
 453 **and D).**

454

#### 455 4.3 A double-layer structure in NLC

456 The third early result addresses a double-layer event in NLC observed over Greenland on 25 June 2024. The  
 457 reader is recommended to look at the video of NLC image sequence at 05:08-06:49 UTC (02:35-04:08 LST) on  
 458 25 June (<https://doi.org/10.7910/DVN/AKJK4P>). One can see at least two NLC layers moving in opposite  
 459 directions: one cloud layer visually moved approximately from the top to the bottom of the image frame,  
 460 whereas another cloud layer moved in the opposite direction from the bottom to the top. Double-layer and  
 461 multiple-layer structures in NLC/PMC have been previously observed and modeled in a number of studies  
 462 (Baumgarten et al., 2012; Dubinskii and Popel, 2012; Kaifler et al., 2013; Gao et al., 2017; Li et al., 2017).

463 We have carefully estimated speeds and directions of seven individual NLC points in each of these two  
 464 different layers. **NLC point trace analysis was applied to the original (unfiltered and unprojected) images.**  
 465 **After completing the trace analysis, the estimation of NLC velocities (speeds and directions) was**  
 466 **performed on projected images.** The results of this analysis are as follows. For the NLC layer visually moving  
 467 from the bottom to the top, the average NLC speed was about 28 m/s, with the average azimuth of about 18°  
 468 (counting clockwise from the north). For the NLC layer moving from the top to the bottom, the average NLC  
 469 speed was about 60 m/s, with the average azimuth of about 193°. These statistical results are summarized in  
 470 Table 1 as well as shown in Fig. 12, demonstrating NLC velocity vectors (green and yellow arrows) estimated  
 471 for the two different layers. Note that we have taken into account the velocity vector of the TRANSAT flight  
 472 (zonal and meridional speed was -10.5 m/s and -7.1 m/s, respectively) when calculating these NLC wind  
 473 velocities vectors. To calculate NLC speeds, the average height of the entire cloud layer was chosen as 83 km.  
 474 Uncertainty in the height of the NLC layers between 82 and 86 km gives an error of 3-4% of the average NLC  
 475 speed.

476 It can be assumed that different movements of the two NLC layers were caused by different wind systems  
 477 located at different heights in the mesopause region. We cannot measure the heights of the different NLC layers  
 478 but we can consider a model simulation to check this assumption. We utilize JAWARA zonal and meridional  
 479 wind data in the mesopause region taken at 06:00 UTC on 25 June 2024, i.e., when and where different motions  
 480 of the NLC were observed.

481 JAWARA wind data are shown in Fig. 12 by the vector field as well as by the absolute wind speed (color  
 482 code). Panel A represents JAWARA wind data at the pressure level of 0.0042 hPa (~82.9 km) above Greenland  
 483 and seven NLC velocity vectors (green arrows) observed in the NLC layer which was moving in the NNE  
 484 direction (visually from the bottom to the top). The average wind speed was about 21 m/s in the direction of 13°  
 485 (counting clockwise from the north) in the vicinity of the observed NLC. Panel B illustrates JAWARA wind data  
 486 at the pressure level of 0.0017 hPa (~86.8 km). One can see about the opposite direction (to SSW) of the model  
 487 wind field to that shown on panel A. The average JAWARA wind speed was about 56 m/s, with the average  
 488 azimuth of 188°, in the vicinity of the observed NLC. Seven NLC velocity vector are shown by the yellow  
 489 arrows which have about the same speed and the direction of motion. All these statistical data are summarized in

490 Table 1, which demonstrate good agreement between the measured NLC and JAWARA wind velocities both in  
 491 the absolute value and in the propagation direction, taking into account their uncertainties. Note that the  
 492 JAWARA model has a low horizontal spatial resolution ( $2.81^\circ$  or  $\sim 310$  km in latitude and  $\sim 113$  km in longitude  
 493 in the analyzed space domain over Greenland) and cannot reproduce wave dynamics due to small-scale gravity  
 494 waves. However, in this particular case, the JAWARA model does correspond well to the observed motions of  
 495 the two different NLC layers.

496

497 **Table 1.** Statistical parameters of the movement of two different layers observed in NLC during the TRANSAT  
 498 balloon flight on 25 June 2024. For comparison, wind data from the JAWARA model are shown. Uncertainties  
 499 represent one standard deviation.

Two NLC layers oppositely moved in image frame	NLC speed (m/s)	NLC azimuth (degree from north)	JAWARA wind speed (m/s)	JAWARA wind azimuth (degree from north)
From bottom to top	$27.8 \pm 10.0$	$18.2 \pm 8.2$	$21.0 \pm 3.7$ at 0.0042 hPa	$13.0 \pm 12.0$ at 0.0042 hPa
From top to bottom	$60.5 \pm 11.3$	$192.5 \pm 2.2$	$56.1 \pm 2.5$ at 0.0017 hPa	$188.0 \pm 4.3$ at 0.0017 hPa

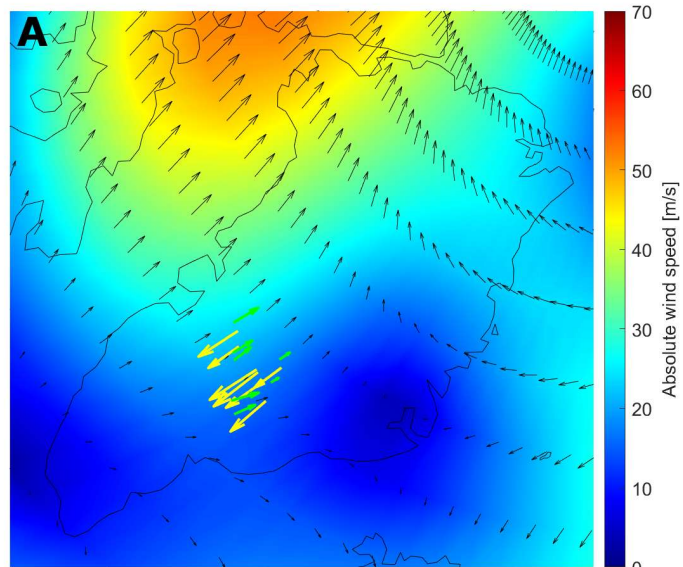
500

501 Panel C of Fig. 4+ 12 shows the JAWARA wind velocity vector as a function of altitude for a specific point  
 502 in the vicinity of the observed NLC. The cyclic rotation of the wind velocity vector is clearly seen between 80  
 503 and 94 km altitude, i.e., there was a circular rotation of the wind vector along the azimuth of  $360^\circ$ . Panel D  
 504 illustrates the corresponding hodograph of the tip of the horizontal wind vector with the subtracted mean velocity  
 505 values ( $-33$  m/s and  $-18$  m/s for the zonal and meridional wind component, respectively) between 80 and 94 km,  
 506 that is, perturbations of the horizontal wind velocity. It is well known that a gravity wave induces horizontal  
 507 wind variations rotating, in general, elliptically with height, and hodograph analysis is commonly used to derive  
 508 gravity wave parameters (Gossard and Hooke, 1975; Eckermann, 1996 and references therein). In the present  
 509 case, the hodograph has an almost circular form, implying near circular polarization ( $P \approx 0$ ). Perturbations of the  
 510 horizontal wind are of 45-50 m/s, and the perturbation vector has a clockwise rotation with increasing height  
 511 which means that the group velocity of this particular gravity wave was propagating upward (phase velocity was  
 512 downward). Such an inertia-gravity wave could indeed generate winds in different directions in the given  
 513 volume of the mesopause, forming a multiple-layer structure from a single NLC layer. The inertia-gravity wave  
 514 interpretation is a plausible scenario which is consistent with JAWARA winds and NLC motions. At the same  
 515 time, it should be noted that the background wind in the mesopause region abruptly changes its speed and  
 516 direction with altitude in summer (Portnyagin and Solovjova, 2000; Conte et al., 2025). Therefore, other  
 517 mechanisms such as the vertical displacement of the NLC layer by gravity waves, may provide the observed  
 518 different NLC motions.

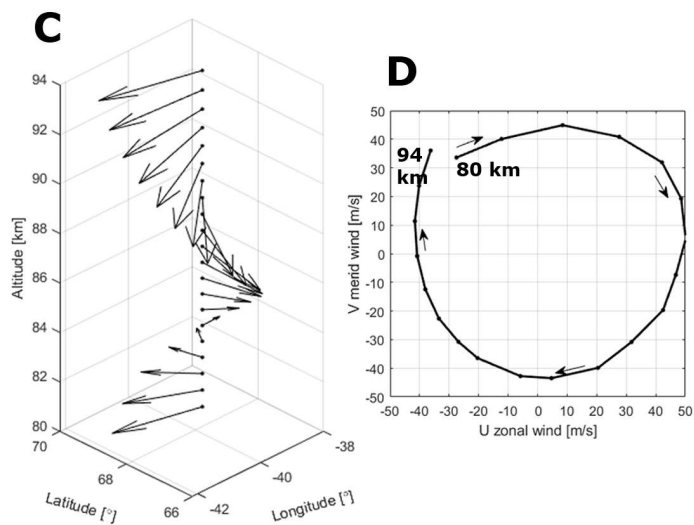
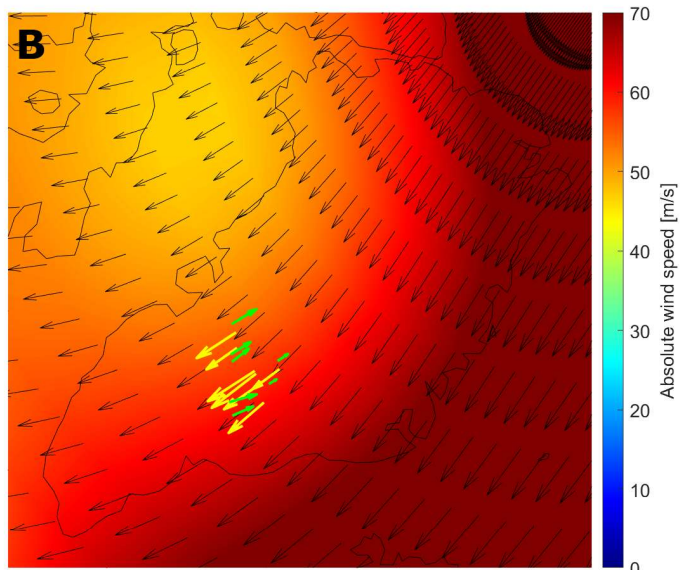
519 It is important to note the following. The clockwise wind rotation with altitude by JAWARA was the  
 520 opposite of that found by Conte et al. (2025), who have analyzed long-term meteor radar measurements in the  
 521 mesopause region at high latitudes over northern Norway. The authors have obtained the counter-clockwise  
 522 rotation of the mean wind speed with altitude in the summer time. The same effect of the wind rotation with  
 523 altitude is predicted by the global empirical wind model for the upper mesosphere/lower thermosphere  
 524 (Portnyagin and Solovjova, 2000). In this present case, the clockwise rotation of the wind speed indicates the

525 dominance of the inertia-gravity wave over the mean wind rotation speed in the space-time domain under  
526 consideration. Also, we should note that even without inertia-gravity waves, winds in the mesopause region can  
527 rotate with altitude (Ekman spiral) under the action of the Ekman-type mechanism involving Coriolis force and  
528 turbulent viscosity (Chkhetiani and Shalimov, 2010; 2022).  
529

JAWARA Wind on 2024-06-25 at 06 UTC at 0.0042 hPa  $\sim$ 82.9 km



JAWARA Wind on 2024-06-25 at 06 UTC at 0.0017 hPa  $\sim$ 86.8 km



530

531 **Figure 11** **12**: JAWARA wind data (thin black arrows) at the pressure level of 0.0042 hPa,  $\sim$ 82.9 km (A) and at

532 the pressure level of 0.0017 hPa,  $\sim$ 86.8 km (B) at 06 UTC on 25 June 2024. The color code is the absolute

533 horizontal wind speed. The green and yellow arrows show velocities of NLC moving in opposite directions (see  
 534 the text). (C) JAWARA wind velocity vector selected for a specific location (68.4°N, 39.4°W) as a function of  
 535 altitude between 80 and 94 km. (D) Hodograph of disturbances of the horizontal wind velocity vector between  
 536 80 and 94 km. The thin arrows show the direction (clockwise rotation) of wind velocity disturbances with  
 537 altitude.

538

## 539 5 Conclusions

540 Observations of noctilucent clouds were performed from the stratosphere during the TRANSAT transatlantic  
 541 long-duration balloon flight between Sweden and Canada on 22-26 June 2024. NLC were observed with the  
 542 SONC imager composed of three high-resolution SONY  $\alpha$ 7 Mark III cameras, stabilized on the TRANSAT  
 543 gondola. NLC cannot be detected by an imager from the ground during the midnight Sun season due to strong  
 544 background scattering in the lower atmosphere. However, an observation from the stratosphere can detect NLC  
 545 during 24 hours. These **Stratospheric** measurements offer an unprecedented view of mesospheric cloud  
 546 dynamics on small- and large-scales, bridging the observational gap between ground-based and satellite  
 547 platforms. The main results of this study can be summarized as follows:

- 548 1. One wide-angle camera was completely operational during the whole flight for 3.8 days, taking a total of  
 549 40,000 images, of which about 6200 images are suitable for scientific analysis.
- 550 2. NLC were detected nearly continuously during the whole flight, showing a strong variability in space and  
 551 time. The dominant role of solar thermal tides in the summer mesopause decreases when NLC are observed  
 552 on large scales of about 1500 km. At such scales, gravity waves of various scales from 1 to several hundred  
 553 km play the largest role, evolving and modulating NLC layers in different regions of the polar mesopause.  
 554 Note that this result was obtained on the basis of a single 3.8-day flight and a limited range of latitudes (60-  
 555 75°N) and longitudes (45°E-95°W). Thus, the present case study cannot claim to be a general statement  
 556 about the relative importance of solar tides compared to gravity waves.
- 557 3. Ground-based support of the TRANSAT balloon campaign was represented by two lidars located at Esrange  
 558 and Andoya. Both lidars registered NLC at the time of the initial phase of the balloon flight over northern  
 559 Scandinavia. The NLC layered was continuous from 20 UTC on 22 June until 09 UTC on 23 June,  
 560 modulated in height between 81 and 86 km, and showing a double-layer structure.
- 561 4. The same mesospheric cloud layer was recorded from the stratosphere and space around noon on 25 June  
 562 2024. Such a simultaneous common-volume NLC detection was carried out, for the first time, using a limb-  
 563 geometry by the MATS satellite. The extended cloud layer was observed over at least Greenland, Baffin Bay  
 564 and Baffin Island, with part of this layer registered from the stratosphere over the west coast of Greenland  
 565 and Baffin Bay. Images from the stratosphere showed complex wave dynamics, with interference of small-  
 566 scale waves and turbulent regions below what MATS can partly resolve. Therefore, observations of clouds  
 567 from the stratosphere and space, using limb geometry, complement each other well.
- 568 5. Gravity waves had characteristic horizontal wavelengths of 30-40 km for the case study considered in the  
 569 mesopause over Greenland on 25 June 2024.
- 570 6. One peculiar case of the NLC disappearance in the polar mesopause in the afternoon of 24 June 2024 has  
 571 been analyzed. This cloud disappearance was caused by the localized warm spot in the mesopause region

572 between Greenland and Scandinavia, as shown by Aura/MLS satellite and JAWARA model data. This warm  
573 spot in the mesopause region was caused by the intrusion of a warm air mass from middle to high latitudes.

574 7. Different movements of NLC were observed in the morning of 25 June 2024 over Greenland. One part of the  
575 clouds moved to NNE, another one moved to SSW. A detailed analysis of wind data based on the JAWARA  
576 model showed that there were different wind systems between 80 and 94 km altitude over Greenland, with a  
577 clockwise wind rotation with altitude. Most likely, a large inertia-gravity wave propagated upwards, causing  
578 significant disturbances (45-50 m/s) of the horizontal wind. The wind disturbances caused NLC to move  
579 differently at different altitudes. Other mechanisms such as the vertical displacement of the NLC layer by  
580 gravity waves may explain the observed different NLC motions.

581 These results demonstrate the scientific value of long-duration stratospheric balloon missions for  
582 mesospheric research. Future campaigns of this type will benefit from expanded multi-spectral imaging, real-  
583 time data transmission, and coordinated ground-satellite observations to further improve understanding of  
584 mesospheric cloud dynamics. A statistical analysis of the wave dynamics observed in NLC during the 2024  
585 TRANSAT balloon flight, and investigation of microphysical properties of NLC ice particles will be addressed  
586 in future studies.

587

#### 588 **Data availability**

589 Two video files of the SONC experiment are available on the Harvard Dataverse repository  
590 (<https://doi.org/10.7910/DVN/AKJK4P>; <https://doi.org/10.7910/DVN/1PHRZU>). Individual NLC images taken  
591 from the stratosphere by the SONC experiment that support the findings of this study are available at the  
592 HEMERA Data Centre (<https://data.hemera-h2020.eu/atmospheric-balloon-experiments/#/>) as well as will be  
593 made available on request.

594

#### 595 **Author contributions**

596 PD, HS, NP, VP, JK and AR have designed two balloon-borne experiments dedicated to studies of noctilucent  
597 clouds and infrasound waves. PD wrote the draft of the paper and made analyses of the SONC images, Esrange  
598 lidar, Aura/MLS and JAWARA data. LM made analysis of the MATS satellite data. PV and JH performed  
599 Esrange lidar measurements. GB performed ALOMAR lidar measurements. DE designed and produced the  
600 electric control unit for the SONC imager. All authors discussed the results and contributed to revisions of the  
601 text and the figures.

602

#### 603 **Competing interests**

604 The contact author has declared that none of the authors has any competing interests.

605

#### 606 **Acknowledgments**

607 The authors thank the CNES/INSU-CNRS Balloon Programme. The TRANSAT balloon flight was funded and  
608 performed by the French Space Agency (CNES). The authors thank the Aura/MLS team for providing  
609 temperature and water vapor data around the globe during the 2024 TRANSAT balloon flight.

610

#### 611 **Financial support**

612 The SONC imager hardware (imager and electronic control unit) was funded by the Kempe Foundation  
 613 (Kempestiftelserna) under grant agreement JCK-1901.4. The infrasound instrument and flight costs of the SONC  
 614 and infrasound instruments were financed under research grant 42/17 from the Swedish National Space Agency  
 615 (Rymdstyrelsen). The MATS satellite and JH were financed by the Swedish National Space Agency under grant  
 616 2021-00052. LM was financed by the Swedish National Space Agency under grant 2022-00108 and the Swedish  
 617 Research Council (Vetenskapsrådet) under grant 2021-04876.

618

619 **References**

620 Bailey, S. M., Thomas, G. E., Rusch, D. W., Merkel, A. W., Jeppesen, C., Carstens, J. N., Randall, C. E.,  
 621 McClintock, W. E., and Russell, J. M.: Phase functions of polar mesospheric cloud ice as observed by the CIPS  
 622 instrument on the AIM satellite, *J. Atmos. Sol.-Terr. Phys.*, 71, 3-4, 373–380.

623 <http://dx.doi.org/10.1016/j.jastp.2008.09.039>, 2009.

624 Baumgarten, G., and Fritts, D. C.: Quantifying Kelvin-Helmholtz instability dynamics observed in  
 625 noctilucent clouds: 1. Methods and observations, *J. Geophys. Res. Atmos.*, 119, 9324–9337,  
 626 doi:10.1002/2014JD021832, 2014.

627 Baumgarten, G., Chandran, A., Fiedler, J., Hoffmann, P., Kaifler, N., Lumpe, J., Merkel, A., Randall, C. E.,  
 628 Rusch, D., and Thomas, G.: On the horizontal and temporal structure of noctilucent clouds as observed by  
 629 satellite and lidar at ALOMAR (69N), *Geophys. Res. Lett.*, 39, L01803, doi:10.1029/2011GL049935, 2012.

630 Baumgarten, G.: Doppler Rayleigh/Mie/Raman lidar for wind and temperature measurements in the middle  
 631 atmosphere up to 80 km, *Atmos. Meas. Tech.*, 3, 1509-1518. doi:10.5194/amt-3-1509-2010, 2010.

632 Baumgarten, G., Fiedler, J., Fricke, K. H., Gerding, M., Hergig, M., Hoffmann, P., et al.: The noctilucent  
 633 cloud (NLC) display during the ECOMA/MASS sounding rocket flights on 3 August 2007: morphology on  
 634 global to local scales, *Ann. Geophys.*, 27, 953–965, 2009.

635 Blum, U., and Fricke, K. H.: The Bonn University lidar at the Esrange: technical description and capabilities  
 636 for atmospheric research, *Ann. Geophys.*, 23, 1645–1658, 2005.

637 Chkhetiani, O., and Shalimov, S.: On anomalous wind amplitudes in the lower ionosphere, *J. Atmos. Sol.-*  
 638 *Terr. Phys.*, 240, 105960, <https://doi.org/10.1016/j.jastp.2022.105960>, 2022.

639 Chkhetiani, O. G., and Shalimov, S. L.: Helicity in the upper atmosphere and Ekman-type instabilities, *Dokl.*  
 640 *Earth Sc.*, 431, 345–350, <https://doi.org/10.1134/S1028334X10030177>, 2010.

641 Conte, J. F., Chau, J. L., Renkowitz, T., Latteck, R., Tsutsumi, M., Jacobi, C., Gulbrandsen, N., and Nozawa,  
 642 S.: Observing mesoscale dynamics with multistatic specular meteor radars: first climatology of momentum flux,  
 643 horizontal divergence and relative vorticity over northern central Europe, *Ann. Geophys.*, 43, 603–619,  
 644 <https://doi.org/10.5194/angeo-43-603-2025>, 2025.

645 Dalin, P., Suzuki, H., Pertsev, N., Perminov, V., Efremov, D., Voelger, P., Narayanan, V. L., Mann, I.,  
 646 Häggström, I., Zalcik, M., Ugolnikov, O., Hedin, J., Gumbel, J., Latteck, R., and Baumgarten, G.: Studies of  
 647 noctilucent clouds from the stratosphere during the SONC balloon-borne experiment in 2021. *J. Atmos. Sol.-*  
 648 *Terr. Phys.*, 240, 105959, doi.org/10.1016/j.jastp.2022.105959, 2022.

649 Dalin, P., Pertsev, N., Perminov, V., Efremov, D., and Romejko, V.: Stratospheric observations of  
 650 noctilucent clouds: a new approach in studying middle- and large-scale mesospheric dynamics, *Ann. Geophys.*,  
 651 38, 61–71, <https://doi.org/10.5194/angeo-38-61-2020>, 2020.

- 652 Dalin, P., Pertsev, N., Perminov, V., Efremov, D., and Romejko, V.: Looking at “night-shining” clouds from  
 653 the stratosphere, *Eos–AGU*, 100, <https://doi.org/10.1029/2019EO118439>, 2019.
- 654 Dalin, P., Pogoreltsev, A., Pertsev, N., Perminov, V., Shevchuk, N., Dubietis, A., Zalcik, M., et al.: Evidence  
 655 of the formation of noctilucent clouds due to propagation of an isolated gravity wave caused by a tropospheric  
 656 occluded front, *Geophys. Res. Lett.*, 42, 2037–2046, <https://doi.org/10.1002/2014GL062776>, 2015.
- 657 Dalin, P., Pertsev, N., Frandsen, S., Hansen, O., Andersen, H., Dubietis, A., and Balciunas, R.: A case study  
 658 of the evolution of a Kelvin-Helmholtz wave and turbulence in noctilucent clouds, *J. Atmos. Sol.-Terr. Phys.*,  
 659 72, 14-15, 1129-1138, doi:10.1016/j.jastp.2010.06.011, 2010.
- 660 Dalin, P., Pertsev, N., Zadorozhny, A., Connors, M., Schofield, I., Shelton, I., et al.: Ground-based  
 661 observations of noctilucent clouds with a northern hemisphere network of automated digital cameras, *J. Atmos.*  
 662 *Sol.-Terr. Phys.*, 70, 1460–1472, 2008.
- 663 DeLand, M. T., and Thomas, G. E.: Updated PMC trends derived from SBUV data, *J. Geophys. Res. Atmos.*,  
 664 120, 2140-2166, doi:10.1002/2014JD022253, 2015.
- 665 Demissie, T. D., Espy, P. J., Kleinknecht, N. H., Hatlen, M., Kaifler, N., and Baumgarten, G.: Characteristics  
 666 and sources of gravity waves observed in noctilucent cloud over Norway, *Atmos. Chem. Phys.*, 14, 12133–  
 667 12142, doi:10.5194/acp-14-12133-2014, 2014.
- 668 Dubinskii, A. Yu., and Popel, S. I.: Formation and evolution of dusty plasma structures in the ionosphere,  
 669 *JETP Lett.*, 96, 21–26, doi:10.1134/S0021364012130048, 2012.
- 670 Eckermann, S. D.: Hodographic analysis of gravity waves: relationships among Stokes parameters, rotary  
 671 spectra and cross-spectral methods, *J. Geophys. Res.*, 101, 19169–19174, 1996.
- 672 Fiedler, J., Baumgarten, G., Berger, U., Hoffmann, P., Kaifler, N., and Lübken, F.-J.: NLC and the  
 673 background atmosphere above ALOMAR, *Atmos. Chem. Phys.*, 11, 5701–5717. doi:10.5194/acp-11-5701-2011,  
 674 2011.
- 675 **Fritts, D. C., Wang, L., Baumgarten, G., Miller, A. D., Geller, M. A., Jones, G., Limon, M., Chapman,**  
 676 **D., Didier, J., et al.: High-resolution observations and modeling of turbulence sources, structures, and**  
 677 **intensities in the upper mesosphere, *J. Atmos. Sol.-Terr. Phys.*, 162, 57-78,**  
 678 **<https://doi.org/10.1016/j.jastp.2016.11.006>, 2017.**
- 679 Fritts, D. C., Miller, A. D., Kjellstrand, C. B., Geach, C., Williams, B. P., Kaifler, B., et al.: PMC Turbo:  
 680 Studying gravity wave and instability dynamics in the summer mesosphere using polar mesospheric cloud  
 681 imaging and profiling from a stratospheric balloon, *J. Geophys. Res. Atmos.*, 124, 6423–6443.  
 682 <https://doi.org/10.1029/2019JD030298>, 2019.
- 683 Froidevaux, L., Livesey, N. J., Read, W. G., Jiang, Y. B., Jiménez, C. C., Filipiak, M. J., Schwartz, M. J., et  
 684 al.: Early validation analyses of atmospheric profiles from EOS MLS on the Aura satellite, *IEEE Transactions on*  
 685 *Geoscience and Remote Sensing*, 44, 5, 1106-1121, 2006.
- 686 Gadsden, M., and Schröder, W.: *Noctilucent Clouds*, Springer, New York, 1989.
- 687 Gao, H., Shepherd, G. G., Tang, Y., Bu, L., and Wang, Z.: Double-layer structure in polar mesospheric  
 688 clouds observed from SOFIE/AIM, *Ann. Geophys.*, 35, 295–309, <https://doi.org/10.5194/angeo-35-295-2017>,  
 689 2017.
- 690 Gossard, E. E., and Hooke, W. H.: *Waves in the atmosphere: atmospheric infrasound and gravity waves –*  
 691 *their generation and propagation*, Elsevier Scientific Publishing Co, Amsterdam, 1975.

- 692 Gumbel, J., Megner, L., Christensen, O. M., Ivchenko, N., Murtagh, D. P., Chang, S., Dillner, J., Ekebrand, T.,  
693 Giono, G., Hammar, A., Hedin, J., et al.: The MATS satellite mission – gravity wave studies by Mesospheric  
694 Airglow/Aerosol Tomography and Spectroscopy, *Atmos. Chem. Phys.*, 20, 431–455, [https://doi.org/10.5194/acp-](https://doi.org/10.5194/acp-20-431-2020)  
695 [20-431-2020](https://doi.org/10.5194/acp-20-431-2020), 2020.
- 696 Gumbel, J., and Witt, G.: Rocket-borne photometry of NLC particle populations, *Adv. Space Res.*, 28, 7, 1053-  
697 1058, 2001.
- 698 Kaifler, N., Baumgarten, G., Klekociuk, A. R., Alexander, S. P., Fiedler, J., and Lübken, F.-J.: Small scale  
699 structures of NLC observed by lidar at 69°N/69°S and their possible relation to gravity waves, *J. Atmos. Sol.-*  
700 *Terr. Phys.*, 104, 244–252, doi:10.1016/j.jastp.2013.01.004, 2013.
- 701 Karlsson, B., and Gumbel, J.: Challenges in the limb retrieval of noctilucent cloud properties from  
702 Odin/OSIRIS, *Adv. Space Res.*, 36, 935-942, doi:10.1016/j.asr.2005.04.074, 2005.
- 703 Koshin, D., Sato, K., Miyazaki, K., and Watanabe, S.: An ensemble Kalman filter data assimilation system  
704 for the whole neutral atmosphere, *Geosci. Model Dev.*, 13, 3145–3177, [https://doi.org/10.5194/gmd-13-3145-](https://doi.org/10.5194/gmd-13-3145-2020)  
705 [2020](https://doi.org/10.5194/gmd-13-3145-2020), 2020.
- 706 Koshin, D., Sato, K., Kohma, M., and Watanabe, S.: An update on the 4D-LETKF data assimilation system  
707 for the whole neutral atmosphere, *Geosci. Model Dev.*, 15, 2293–2307, [https://doi.org/10.5194/gmd-15-2293-](https://doi.org/10.5194/gmd-15-2293-2022)  
708 [2022](https://doi.org/10.5194/gmd-15-2293-2022), 2022.
- 709 Koshin, D., Sato, K., Watanabe, S., et al.: The JAGUAR-DAS whole neutral atmosphere reanalysis:  
710 JAWARA, *Prog. Earth Planet. Sci.*, 12, 1, <https://doi.org/10.1186/s40645-024-00674-3>, 2025.
- 711 Lambert, A., Read, W. G., Livesey, N. J., Santee, M. L., Manney, G. L., Froidevaux, L., Wu, D. L.,  
712 Schwartz, M. J., Pumphrey, H. C., Jimenez, C., Nedoluha, G. E., et al.: Validation of the Aura Microwave Limb  
713 Sounder middle atmosphere water vapor and nitrous oxide measurements, *J. Geophys. Res.*, 112, D24S36, 2007.
- 714 Li, H., Wu, J., and Zhou, Z.: The formation of multiple layers of ice particles in the polar summer mesopause  
715 region, *Ann. Geophys.*, 34, 117–122, doi:10.5194/angeo-34-117-2016, 2016.
- 716 Liu, X., Yue, J., Xu, J., Yuan, W., Russell III, J. M., Hervig, M. E., and Nakamura, T.: Persistent longitudinal  
717 variations in 8 years of CIPS/AIM polar mesospheric clouds, *J. Geophys. Res. Atmos.*, 121, 8390–8409,  
718 doi:10.1002/2015JD024624, 2016.
- 719 Megner, L., Gumbel, J., Christensen, O. M., Linder, B., Murtagh, D., Ivchenko, N., Krasauskas, L., Hedin, J.,  
720 Dillner, J., and Stegman, J.: MATS satellite images (level 1b) of airglow and noctilucent clouds in the  
721 mesosphere/lower thermosphere, February–May 2023, Dataset version 1.0, Bolin Centre Database,  
722 <https://doi.org/10.17043/mats-level-1b-limb-cropd-1.0>, 2025.
- 723 Miller, A. D., Fritts, D. C., Chapman, D., Jones, G., Limon, M., Araujo, D., et al.: Stratospheric imaging of  
724 polar mesospheric clouds: a new window on small-scale atmospheric dynamics, *Geophys. Res. Lett.*, 42, 6058–  
725 6065, doi:10.1002/2015GL064758, 2015.
- 726 Murphy, D. M., and Koop, T.: Review of the vapour pressures of ice and supercooled water for atmospheric  
727 applications, *Q. J. R. Meteorol. Soc.*, 131, 1539–1565. doi:10.1256/qj.04.94, 2005.
- 728 Pautet, P.-D., Stegman, J., Wrasse, C. M., Nielsen, K., Takahashi, H., Taylor, M. J., et al.: Analysis of gravity  
729 waves structures visible in noctilucent cloud images, *J. Atmos. Sol.-Terr. Phys.*, 73, 14-15, 2082-2090, doi:  
730 10.1016/j.jastp.2010.06.001, 2011.

- 731 Pertsev, N. N., Dalin, P. A., Perminov, V. I., Gusev, N. K., Tsimerinov, E. Yu., Solodovnik, A. A.,  
732 Zadorozhny, A. M., Korotyshkin, D. V., and Bordonskiy, G. S.: Analysis of noctilucent cloud fields according to  
733 ground-based network and airborne photography data, *Izv. Atmos. Ocean. Phys.*, 60, 2, 187–194,  
734 doi.org/10.1134/S0001433824700191, 2024.
- 735 Portnyagin, Y. I. and Solovjova, T. V.: Global empirical wind model for the upper mesosphere/lower  
736 thermosphere. I. Prevailing wind, *Ann. Geophys.*, 18, 300–315, <https://doi.org/10.1007/s00585-000-0300-y>,  
737 2000.
- 738 **Randall, C. E., Carstens, J., France, J. A., Harvey, V. L., Hoffmann, L., Bailey, S. M., Alexander, M.**  
739 **J., Lumpe, J. D., Yue, J., et al.: New AIM/CIPS global observations of gravity waves near 50–55 km,**  
740 ***Geophys. Res. Lett.*, 44, 7044–7052, <https://doi.org/10.1002/2017GL073943>, 2017.**
- 741 Rapp, M., Lubken, F.-J., Müllemann, A., Thomas, G. E., and Jensen, E. J.: Small-scale temperature  
742 variations in the vicinity of NLC: Experimental and model results, *J. Geophys. Res.*, 107, D19, 4392,  
743 doi:[10.1029/2001JD001241](https://doi.org/10.1029/2001JD001241), 2002.
- 744 Read, W. G., Lambert, A., Bacmeister, J., Cofield, R. E., Christensen, L. E., Cuddy, D. T., Daffer, W. H.,  
745 Drouin, B. J., Fetzer, E., Froidevaux, et al.: Aura Microwave Limb Sounder upper tropospheric and lower  
746 stratospheric H<sub>2</sub>O and relative humidity with respect to ice validation, *J. Geophys. Res.*, 112, D24S35, 2007.
- 747 Reimuller, J. D., Thayer, J. P., Baumgarten, G., Chandran, A., Hulley, B., Rusch, D., Nielsen, K., and  
748 Lumpe, J.: Synchronized imagery of noctilucent clouds at the day-night terminator using airborne and  
749 spaceborne platforms, *J. Atmos. Sol.-Terr. Phys.*, 73, 14-15, 2091-2096, 2011.
- 750 Schwartz, M. J., Lambert, A., Manney, G. L., Read, W. G., Livesey, N. J., Froidevaux, L., Ao, C. O.,  
751 Bernath, P. F., Boone, C. D., Cofield, R. E., et al.: Validation of the Aura Microwave Limb Sounder temperature  
752 and geopotential height measurements, *J. Geophys. Res.*, 113, D15S11, 2008.
- 753 Suzuki, H., Matsumoto, A., Dalin, P., Nakamura, Y., Ishii, S., Sakanoi, K., Sakaguchi, K., Takada, T., Tsuda,  
754 T. T., and Hozumi, Y.: Capability of airline jets as an observation platform for noctilucent clouds at middle  
755 latitudes, *Prog. Earth Planet. Sci.*, 9, 11, <https://doi.org/10.1186/s40645-022-00469-4>, 2022.
- 756 Thomas, G.E.: Solar Mesosphere Explorer measurements of polar mesospheric clouds (noctilucent clouds), *J.*  
757 *Atmos. Terr. Phys.*, 46, 9, 819-824, 1984.
- 758 Tsuda, T. T., Hozumi, Y., Kawaura, K., Tatsuzawa, K., Ando, Y., Hosokawa, K., et al.: Detection of polar  
759 mesospheric clouds utilizing Himawari-8/AHI full-disk images, *Earth Space Sci.*, 9,  
760 2021EA002076, <https://doi.org/10.1029/2021EA002076>, 2022.
- 761 Wallis, S., DeLand, M., and Savigny, C.: Did the 2022 Hunga eruption impact the noctilucent cloud season in  
762 2023/24 and 2024?, *Atmos. Chem. Phys.*, 25, 3635–3645. <https://doi.org/10.5194/acp-25-3635-2025>, 2025.
- 763 Zadorozhny, A. M., Tyutin, A. A., Witt, G., Wilhelm, N., Wälchli, U., Cho, J. Y. N., and Swartz, W. E.:  
764 Electric field measurements in the vicinity of noctilucent clouds and PMSE, *Geophys. Res. Lett.*, 20, 20, 2299-  
765 2302, 1993.